

Highlights

Sub-meter resolution canopy height maps using self-supervised learning and a vision transformer trained on Aerial and GEDI Lidar

Jamie Tolan¹, Hung-I Yang¹, Ben Nosarzewski¹, Guillaume Couairon², Huy Vo², John Brandt³, Justine Spore³, Sayantan Majumdar⁴, Daniel Haziza², Janaki Vamaraju¹, Theo Moutakanni², Piotr Bojanowski², Tracy Johns¹, Brian White¹, Tobias Tiecke¹, Camille Couprise²

- 0.5 meter resolution canopy height maps at jurisdictional scale are released.
- Improved performance from Self-Supervised Learning (SSL) and vision transformers.
- First use of SSL and vision transformers for canopy height estimation.
- Low resolution GEDI and high resolution aerial lidar predictions are combined.
- Model generalises well to aerial imagery, even though trained with satellite images.

Sub-meter resolution canopy height maps using self-supervised learning and a vision transformer trained on Aerial and GEDI Lidar

Jamie Tolan¹, Hung-I Yang¹, Ben Nosarzewski¹, Guillaume Couairon², Huy Vo², John Brandt³, Justine Spore³, Sayantan Majumdar⁴, Daniel Haziza², Janaki Vamaraju¹, Theo Moutakanni², Piotr Bojanowski², Tracy Johns¹, Brian White¹, Tobias Tiecke¹, Camille Couprie²

¹ *Meta*; ² *Fundamental AI Research (FAIR), Meta*; ³ *World Resources Institute*; ⁴ *Colorado State University*

Abstract

Vegetation structure mapping is critical for understanding the global carbon cycle and monitoring nature-based approaches to climate adaptation and mitigation. Repeat measurements of these data allow for the observation of deforestation or degradation of existing forests, natural forest regeneration, and the implementation of sustainable agricultural practices like agroforestry. Assessments of tree canopy height and crown projected area at a high spatial resolution are also important for monitoring carbon fluxes and assessing tree-based land uses, since forest structures can be highly spatially heterogeneous, especially in agroforestry systems. Very high resolution satellite imagery (less than one meter (1m) ground sample distance) makes it possible to extract information at the tree level while allowing monitoring at a very large scale. This paper presents the first high-resolution canopy height map concurrently produced for multiple sub-national jurisdictions. Specifically, we produce canopy height maps for the states of California and São Paolo, at sub-meter resolution, a significant improvement over the ten meter (10m) resolution of previous Sentinel / GEDI based worldwide maps of canopy height. The maps are generated by applying a vision transformer to features extracted from a self-supervised model in Maxar imagery from 2017 to 2020, and are trained against aerial lidar and GEDI observations. We evaluate the proposed maps with set-aside validation lidar data as well as by comparing with other remotely sensed maps and field-collected data, and find our model produces

an average Mean Absolute Error (MAE) within set-aside validation areas of 3.0 meters.

Keywords: LIDAR, GEDI, Canopy height, Deep learning, Self-Supervised Learning, Vision Transformers

PACS: 0000, 1111

2000 MSC: 0000, 1111

1. Introduction

Spatially explicit maps of forest vegetation structure, such as tree canopy height and crown projected area, are powerful tools for assessing forest degradation, forest and landscape restoration (FLR), and estimating above-ground woody biomass for carbon emission and sequestration modeling. Existing assessments of the climate implications of woody vegetation flux, including FLR, deforestation, and natural regrowth, often rely on remotely sensed dynamic vegetation models of deforestation and regrowth (Friedlingstein et al. (2019)). Such wall-to-wall data on tree height and canopy structure are used to estimate aboveground woody biomass. However, land-use patterns operate on more granular spatio-temporal scales than those captured by global carbon models, which typically have coarse spatio-temporal resolution. This contributes to the large uncertainty in existing nation-wide and global accounting of carbon stored in forests (Popkin (2015)). Global carbon fluxes associated with forest conversion differ by up to 10 billion metric tons per year when measured by comparing atmospheric carbon and net ocean carbon flux to measurements from long-term forest inventory data (Duncanson et al. (2020)). At a national scale, uncertainty in remotely sensed forest carbon flux increases the uncertainty of reporting country-level avoided emissions, which often rely on coarse sequestration rates for forest types that do not properly account for site-specific variables like height or forest stand age (Yanai et al. (2020)).

Critical to reducing uncertainty in woody carbon models are measurements of forest height and biomass to improve assessments of the spatial variability of carbon removal rates across forest landscapes that have heterogeneous structure (Harris et al. (2021)). Tree height is especially critical to accurately assessing carbon removal rates, as growth rate increases continuously with size, meaning that one large tree can sequester a similar amount of carbon annually as is contained in many medium sized trees (Stephen-

son et al. (2014)). Recent earth observation missions from NASA, namely GEDI and ICESat-2, provide repeated vegetation canopy height maps for the first time. GEDI was launched in December 2018 and collects canopy height and relative height at a 25 meter resolution. ICESat-2 was launched in September 2018 and collects canopy height and relative height at a 13×100 meter native footprint. Recently, multi-sensor fusion has demonstrated potential to improve aboveground biomass mapping (Silva et al. (2021)). To generate wall-to-wall maps of canopy height, researchers commonly combine active optical LiDAR data from ICESat-2 or GEDI with optical imagery from Sentinel-2 or Landsat satellites (Potapov et al. (2021); Lang et al. (2022a); Schwartz et al. (2021); Csillik et al. (2019); Li et al. (2020)).

Our research is motivated by recent literature on woody carbon flux that has evaluated or demonstrated the impact of spatio-temporal variation in vegetation structure on the confidence intervals associated with carbon measurements. For instance, Cook-Patton et al. (2020) produce a global 1-km scale map of potential above-ground carbon accumulation rates by developing machine learning models based on more than 13,000 locations derived from literature. Cook-Patton et al. (2020) find significant variability in predicted carbon accumulation rates compared to defaults from the International Panel on Climate Change (IPCC) at the ecozone scale, suggesting that incorporating spatial variability in carbon dynamics, even at a 1-km scale, can provide a more representative assessment of carbon. In the African tropical montane forests, Cuni-Sanchez et al. (2021) model forest carbon density based on 72,336 measurements of height and tree diameter, identifying two-thirds higher carbon stocks than the IPCC default values for Afromontane forests. These results further suggest that the spatial variability in forest structure contributes greatly to uncertainty in carbon flux modeling.

With regards to specific forest carbon projects, recent research has identified inconsistencies in the crediting processes in part because of coarse resolution carbon sequestration data and inconsistent counterfactual selection processes. Badgley et al. (2022) posit that California's cap-and-trade program over-credits due to comparing projects with average carbon sequestration rates by broad forest types. The comparison of projects with more carbon-dense species against counterfactuals comprising less carbon-dense species overestimates the additionality of the project carbon, resulting in over crediting. The fundamental problem identified by Badgley et al. (2022) is in identifying an ecologically robust point of comparison when project-specific data is compared to coarse, geographically aggregated averages. Similarly,

West et al. (2020) find that the methods to select counterfactual locations greatly impact the estimation of reduced carbon emissions from avoided deforestation in Brazil.

The uncertainty of biomass modelling also affects the uncertainty of the carbon implications of deforestation and regrowth. Tree-based FLR, including agroforestry, reforestation, natural regeneration, and enrichment planting, is considered to be a cost-effective natural climate solution for adaptation and mitigation. However, evaluating the effectiveness of FLR interventions at a large scale is difficult due to its highly distributed nature, typically being practiced on individual land parcels by respective land owners. While carbon reporting frameworks exist for FLR, for example through verified carbon markets, such data are highly project-specific owing to their reliance on intensive manual field measurements. On the other hand, while global maps of forest canopy height exist (Potapov et al. (2021); Lang et al. (2022b)), they are unlikely to be spatially granular enough to describe tree canopy structure on FLR interventions, which require at a minimum measurements of the distribution of canopy height and density as well as tree canopy extent. This is especially the case for FLR interventions with considerable species diversity or multiple vegetation canopies, such as intercropped agroforestry or natural regeneration. For instance, Tesfay et al. (2022) found that 70% of the shade trees in an agroforestry system in Ethiopia were below 3 meters in height, while 3% were above 12 meters in height, with more than a two-order of magnitude range of per-tree carbon stocks depending on tree size.

While FLR monitoring has historically depended on field inventory plots, the massive scale of global FLR ambitions require new paradigms for monitoring, to which improved remote sensing data is central (de Almeida et al. (2020)). Owing to the importance of vegetation structure variability to assessing FLR, recent research has focused on applications of ground lidar or drone-borne lidar to map biomass through the proxies of crown projected area and vegetation height (Almeida et al. (2019b,a)). In the Brazilian Atlantic Forest, de Almeida et al. (2021) demonstrate that drone-borne lidar and hyperspectral imagery are able to map species diversity and biomass of restored forest systems, with lidar data better predicting biomass than hyperspectral imagery. Comparing VHR imagery and lidar data, Dalagnol et al. (2019) demonstrate that automated analyses of VHR imagery capture 60% of deforestation events, while automated analyses of lidar imagery capture 97% of deforestation events in an Amazonian forest. Despite the clear advantages of lidar information for mapping vegetation structure, and the

demonstrated applications of establishing algorithmic relationships between optical and lidar data (Potapov et al. (2021); Lang et al. (2022a)), a gap in the literature remains in modeling tree canopy height by establishing algorithmic relationships between VHR imagery and airborne lidar survey data.

Understanding the importance of highly spatially explicit vegetation structure mapping to both large-scale carbon modeling and project-specific avoided deforestation and restoration monitoring, the objective of this study is to produce high resolution canopy height maps that are able to scale and generalize to large geographies. In this work, we take advantage of the latest advances in computer vision to generate half-meter canopy height maps. Our method consists of an image encoder-decoder model, where low spectral dimensional input images are transformed to a high dimensional encoding and subsequently decoded to predict per-pixel canopy height. We employ self-supervised learning to generate universal and generalizable encodings from the input imagery (Oquab et al., 2023), and train a dense vision transformer (Ranftl et al., 2021) to generate canopy height predictions based on aerial and spaceborne lidar data. We present canopy height maps for the states of São Paulo, Brazil, and California, USA, and provide qualitative and quantitative uncertainty estimates.

Related works on Canopy height prediction

A number of recent studies have utilized aerospatial lidar data from GEDI and ICESat-2 to produce canopy height maps in combination with multispectral optical imagery. Among them, Potapov et al. (2021) combined GEDI RH95 (95th percentile of Relative Height) data with Landsat data to establish a global map at 30 meter resolution, using a bagged regression tree ensemble algorithm. More recently, Lang et al. (2022a), produced a global canopy height map at a 10-meter resolution, applying an ensemble of convolutional neural network (CNN) models to Sentinel-2 imagery to predict the GEDI RH95 footprint. Other works such as Schwartz et al. (2021) focus on smaller regions, managing to produce 10-meter resolution maps. At a national scale, Csillik et al. (2019) generate biomass maps in Peru by applying gradient boosted regression trees between 3.7 meter Planet Dove imagery and airborne lidar, with low uncertainty in dense forests but large amounts of uncertainty in transitional landscapes and areas that are hotspots of land use change. Focusing on a deciduous forest in China, Li et al. (2020) generate 250-meter maps of canopy height based on airborne lidar surveys by

fusing Sentinel-1, Sentinel-2, Landsat, and ICESat-2 observations and modeling with a multi-layered perceptron. Recently, Liu et al. (2023) computed a canopy height map (CHM) map of Europe using 3 meter precision imagery, training two UNets to predict tree extent and CHM using lidar observations and previous CHM predictions from the literature.

Related works on Self-Supervised Learning

We employ the approach of Oquab et al. (2023) to learn universal features in a self-supervised way from satellite images. This approach builds on the vision transformer Self-Supervised Learning (SSL) approaches referred to as DINO (Caron et al. (2021); Zhou et al. (2022)) by introducing techniques to scale them to very large vision datasets. The work of Oquab et al. (2023) trains a teacher model that accesses entire images, and a student model that receives only image crops and masked patches. The SSL objective is to minimize the entropy between the teacher and the student features, leading to state-of-the-art performance in several computer vision tasks, such as image classification, depth prediction, and segmentation. In the context of satellite image analysis, Sirko et al. (2021) employ self-supervised learning to improve the accuracy of building segmentation in Africa. More recently, also leveraging vision transformers, Reed et al. (2022) scale the Masked Auto-Encoder approach of He et al. (2022) and apply it to building segmentation.

Related works on transformers

Transformers are a deep learning approach to encoding low-dimensional input into a high dimensional feature space. In contrast to convolutional neural networks (CNNs), which subsequently apply local convolutional operations to enable the modelling of increasingly long-range spatial dependencies, transformers utilize self-attention modules to enable the modeling of global spatial dependencies across the entire image input (Dosovitskiy et al. (2021)). While increasingly deep CNN models can enable large receptive fields, Luo et al. (2016) demonstrate that the effective receptive fields of CNN models have Gaussian distributions, limiting the ability for CNNs to model long-range spatial dependencies. For dense prediction tasks on high resolution imagery where objects can be many hundreds to thousands of pixels in size, the ability of transformers to model global information is promising. Among the applications to aerial imagery, the work of Xu et al. (2021) uses a Swin transformer to classify high-resolution land cover. Finding that a baseline transformer model struggled with edge detection, Xu et al. (2021) utilized

a self-supervised edge extraction and enhancement method to improve definition of class edges. Wang et al. (2022) utilize the vision transformer architecture as a feature encoder, and apply a feature pyramid decoder to the resulting multi-scale feature maps. Gibril et al. (2023) segment individual date palm trees by applying vision transformers to 5- to 30-cm drone-based imagery, finding that the Segformer architecture improves generalizability to different resolution imagery when compared to CNN-based models.

2. Lidar and optical imagery processing methods

2.1. Satellite Image Dataset Description

Maxar Vivid2 mosaic imagery¹ served as input imagery for model training and inference. This dataset provides global coverage by mosaicing together imagery from multiple instruments (WorldView-2 (WV 2), WorldView-3 (WV 3), Quickbird II) and observation dates. By starting with this mosaiced imagery, we leveraged the extensive data selection pipeline from Maxar, resulting in imagery that had less than 2% percent cloud cover, a global revisit rate predominately (more than 75%) below 36 months (imagery dates from 2017 to 2020 are utilized in this dataset), view angles of less than 30 degrees off nadir, and sun angle of less than 60 degrees from zenith. This imagery consisted of three spectral bands: Red, Green, and Blue (RGB), with approximately a 0.5 meter Ground Sample Distance (GSD). The imagery was processed in the Web Mercator projection (EPSG:3857) and stored with the Bing tiling scheme². Given the high resolution of the original geotiffs, Bing zoom 15 level tiles, with 2048×2048 pixels per tile were used, giving a pixel size of 0.597 meters GSD at the equator.

2.2. Dataset preparation

For easier training and validation of computer vision models, we extracted small regions from the input satellite imagery. Centered around a given location on the earth, a box of fixed ground distance was selected, using a local tangent plane coordinate system. The extracted images at each position had varying dimensions according to their latitude, which were re-sampled to a fixed number of pixels. We typically choose a box side length of 152.7 meters, which, when re-sampled to 256×256 pixel images, provided “thumbnail”

¹<https://resources.maxar.com/data-sheets/imagery-basemaps-data-sheet>

²<https://learn.microsoft.com/en-us/bingmaps/articles/bing-maps-tile-system>

images that matches the lowest resolution (0.597m) of the input imagery described in Section 2.1. Using these thumbnail images both for training and inference ensured that the dataset had constant number of pixels and that the pixel size was the same for all latitudes, preventing potential biases with latitude which may be introduced by variation in pixel size.

2.3. Training Dataset Description

Our approach to the problem of scalable canopy height estimation aimed to leverage two domains of reference height data: densely sampled aerial lidar and sparsely sampled space-based lidar, along with a self-supervised algorithm. Full details the model will be discussed in Section 3, but in brief, the model utilized three sets of optical and lidar data: (1) Unlabeled optical RGB images, used for self-supervised pre-training, (2) aerial lidar Canopy Height Maps (CHM), used to train a transformer from SSL features, and (3) GEDI Relative Height (RH) measurements, used for coarse resolution correction of CHMs. In this section, we describe the datasets used in these three steps.

2.3.1. GEDI Dataset

The GEDI instrument is a full waveform lidar instrument aboard the International Space Station which has sampled global regions between 51.6° N & S latitude with a ~25m beam footprint at ground surface. The instrument details are described in Dubayah et al. (2020), and its measurements of canopy height are described in Dubayah et al. (2022). We used the GEDI L4A Version 2 product and filtered the dataset to reduce noise by only including data which had: degrade flag = 0, surface flag = 1, solar elevation < 0, and sensitivity > 0.95. After this filtering, we were left with a total sample size of 1.3×10^9 measurements. We used the 95th percentile of relative height (RH95) that we paired to 128 × 128 pixel (76 × 76 meter) satellite images from Maxar. These images were processed as described in Section 2.2, but were sized to better match the approximately 25m GEDI beam width.

2.3.2. SSL Dataset

For training the self-supervised encoder, we randomly sampled 3.5 million 256 × 256 pixel satellite thumbnail images which were co-located with the GEDI measurements. No labels were used for the SSL stage.

2.3.3. Aerial Lidar Survey (ALS) Datasets

We gathered approximately 5800 canopy height maps (CHM), selected from the National Ecological Observatory Network (NEON) (2022). Each CHM typically consisted of $1\text{km} \times 1\text{km}$ geotiffs, with a pixel size of one meter (1m) GSD, in local UTM coordinates. We selected the sites used in Weinstein et al. (2021) and additionally manually filtered for sites that have CHM imagery that was well registered and mostly free from mosaicing artifacts. Additionally, we selected sites with imagery acquired less than two years from the observation date in the associated Maxar satellite imagery. A complete list of NEON sites used for training and validation is contained in Appendix A.

2.3.4. Linking ALS Data with RGB imagery

A structured dataset was created from the input CHM geotiffs by selecting random point locations (x, y) from within each raster. Next, following the procedure described in Section 2.2, 256×256 pixel thumbnail images were created by reprojecting to a local tangent plane coordinate system. A corresponding RGB image from the satellite image was linked with this image and these pairs of imagery served as the training data for the SSL model.

2.4. Training and Validation datasets

The NEON ALS dataset was split in sets of 80% training images, 10% calibration and 10% set-aside validation images, typically referred to as training/validation/test in the machine learning community. Model training was conducted over epochs sampled from the training dataset. At the completion of each epoch, metrics were computed from a 10% calibration dataset to calibrate the hyperparameters of the model training process. The calibration dataset was drawn from the same set of sites as the training datasets, but from separate $1\text{km} \times 1\text{km}$ geotiffs to ensure non overlapping pixels.

We constructed a set-aside validation dataset from a subset of sites in our NEON dataset, which we call “NEON test”. None of the sites used in the validation dataset were contained in the training or calibration dataset. A list of NEON sites in the validation set appears in Appendix A. We also prepared validation datasets from other publicly available ALS Lidar datasets, outside of the NEON collection. These datasets covered a variety of geographic locations and ecosystems: “CA-Brande” (Brande, 2021) covered a coastal ecosystem in CA, “São Paulo” (Dos-Santos et al., 2019) covered a region in the Brazilian São Paulo State, and “France” (IGN, 2021) contained data for

many forested and agricultural areas in France. Where these datasets were available as CHMs, we directly used the supplied CHMs. However, for the São Paulo datasets, which only contained point cloud datasets, we processed CHMs following the pit-free algorithm (Khosravipour et al., 2014). The pit-free algorithm was also adopted by the NEON team for generating their CHM product, and we find that different input parameters to the pit-free algorithm had negligible impact on the CHM output.

2.5. Data Augmentation

The 256×256 pixel image thumbnail images of RGB and CHM imagery (Section 2.3.3) were augmented at training time. For training CHM predictors, we augmented with random 90 degree rotations, brightness, and contrast jittering. When training the GEDI model, we only used random 90 degree rotations and random horizontal and vertical flips, since the larger volume of data made augmentation less helpful. We found that these augmentations improved model prediction stability across the various Maxar observations in the input dataset.

3. Model and data generation methods

Our goal was to create a model that produces high resolution canopy height maps and generalizes across large geographic scales. To accomplish that goal, we leveraged the relative strengths of two types of lidar data. Aerial lidar provided high resolution canopy height estimation, but lacks global spatial coverage. In comparison, GEDI has nearly global coverage of transects, but its beam width of approximately 25 meters did not allow for the identification of individual trees. We therefore propose a hybrid approach, where the ALS data provided the detailed spatial information matching the resolution of the input imagery, while GEDI provided the large scale height estimate with global coverage. In this section we describe how we constructed an CHM prediction model that combined these two datasets.

After pre-training on satellite images globally, our high-resolution ALS CHM prediction model was trained on images from the NEON dataset, which contained spatial coverage from sites only within the United States. We expect this ALS CHM model to perform well on ecosystems similar to the training set. To improve generalization of other ecosystems and locations, a low resolution CHM model was independently trained on global GEDI data. The GEDI model was used to compute a rescaling factor map (Section 3.3),

which adjusted the predictions made by the ALS CHM model, as detailed in Section 3.2 and Figure 2.

3.1. Large scale canopy height estimation using GEDI

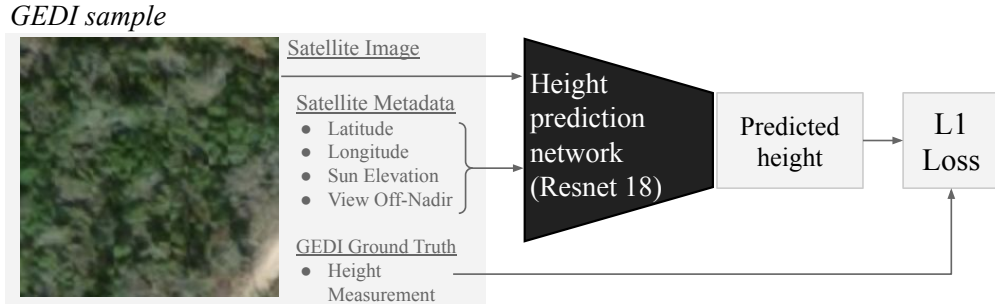


Figure 1: Overview of our methodology to generate predicted RH95 values using GEDI measurements across the globe.

The GEDI prediction model was a simple convolution network, containing five ConvNet layers, followed by five fully connected layers. The inputs to the model were 128×128 pixel Maxar images containing three RGB bands, in topocentric coordinates, processed as described in Section 2.2. The ground truth data consisted of 13 million GEDI measurements, which were randomly sampled from the full GEDI dataset described in Section 2.3.1. The GEDI measurements were split into a 80/10/10% train/calibration/set-aside validation subsets. During training, the samples were drawn with a weight inversely proportional to the natural log of the total number of global samples in its RH95 bin. We find that this sampling method provided a good number of training sample from higher canopy height locations while not overly biasing the model towards ecosystems with the highest canopy heights. After the convolutional layers, we also input a collection of scalar values, designated as “Satellite Metadata” in Figure 1. This metadata included: the latitude, longitude position of each image, the off-nadir view angle of the satellite, the angle between zenith and sun position at capture, and the terrain slope (Mapzen, 2017) of the image footprint. We trained the GEDI model to output a single scalar value, with a L1 loss on a regression task against the RH95 value from the GEDI instrument.

3.2. High resolution canopy height estimation using ALS

The high resolution ALS model was trained independently of the low resolution model. We used the reference dataset described in Section 2.3.3, prepared following the methods described in Section 2.2. The output of the ALS model was a raster of predicted canopy heights at the same resolution as the input imagery. The following two Sections (3.2.1, 3.2.2) describe the two separated approaches we evaluated for building a high resolution model.

3.2.1. SSL-based approach

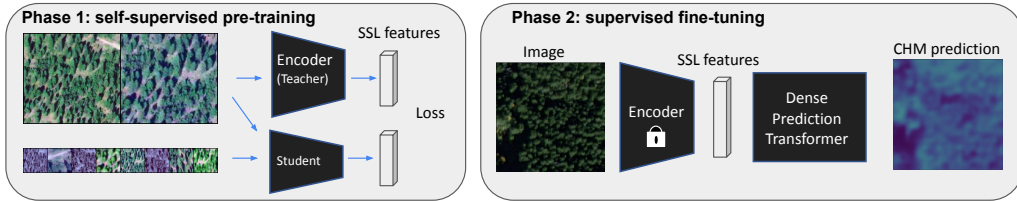


Figure 2: Overview of our SSL approach for generating ALS-based CHMs. During the first stage, we employed the self-supervised learning approach Oquab et al. (2023) leading to a general purpose image encoder. In the second phase, we trained another transformer network to predict CHMs.

Following the recent success of self-supervised learning on dense prediction tasks from Oquab et al. (2023), we employed a self-supervised learning step on worldwide Maxar satellite images to obtain an image encoder delivering features specialized to vegetation images. For the second, supervised decoder stage, we used the ALS CHM data described in Section 2.3.3 to “fine-tune” the model to create a connection between the SSL features and the full resolution canopy height image. In this second phase, instead of a ResUNet decoder, we fine-tune the obtained features using a more sophisticated decoder based on Dense Prediction Transformer (Ranftl et al. (2021)). This approach is described in Figure 2. Our best results were obtained by freezing all layers from the SSL encoder. We employed a one cycle learning rate schedule with a linear warmup in the fine-tuning stage and a “Sigloss” loss function.

Sigloss function. We take advantage from the similarity of canopy height mapping to the task of depth estimation and borrow the loss from Li et al. (2022); Bhat et al. (2021). Given a true canopy height map c and our prediction \hat{c} , the Sigloss is given by

$$\mathcal{L} = \alpha \sqrt{\frac{1}{T} \sum_i \delta_i^2 - \frac{\lambda}{T^2} (\sum_i c_i)^2}, \quad (1)$$

where $\delta_i = \log(\hat{c}_i) - \log(c_i)$, and T is the number of pixels with valid ground truth values. As in previous works, we fix $\lambda = 0.85$ and $\alpha = 10$.

3.2.2. Baseline: ResUNet-based approach

We utilized a ResUNet-18 architecture for our baseline (Zhang et al., 2017), which is an encoder-decoder architecture predicting a $N \times N$ canopy height map from a $3 \times N \times N$ RGB image, with $N = 256$. The baseline model was trained with an L1 loss between the predicted and ground truth CHMs.

When training the ResUNet model, we employed an additional augmentation that simulated opacity and reflectance from cloud cover, for which we replaced the RGB values by white uniformly in the image by a random fraction between 0 to $e^{-0.7}$. We checked that this data augmentation effectively reduced seam lines in produced maps. This augmentation did not bring the same benefits to the SSL results. We also experimented with a Sigloss loss function, however we did not notice improvements in the results from this approach.

3.3. Combining ALS and GEDI model outputs

In this section, we describe the process of connecting our GEDI model outputs (Section 3.1) with ALS model outputs (Section 3.2). Conceptually, the ALS model output provides high resolution canopy estimates but lacks the global context to correctly estimate the absolute height of vegetation in different ecosystems. The first step in making this connection is understanding the relationship between the two sets of lidar data: ALS CHM (Section 2.3.3) and GEDI lidar (Section 2.3.1):

3.3.1. Connection Between ALS p95 and GEDI RH95

To leverage the GEDI model output, we made the following assumption: the GEDI model, on a 128×128 pixel sample, approximates the 95th percentile (p95) of the sample’s ground truth canopy height map. This is justified by running simulations with the the GEDI simulator from Hancock et al. (2019) on the NEON ALS point clouds. The GEDI RH95 measurement used for training the GEDI model corresponds to the 95th percentile

of the lidar's energy response. We simulated the GEDI RH95 values and find that they have excellent correlation ($R^2 = 0.89$) with the p95 of the canopy height map around the corresponding GEDI footprints. This high correlation between GEDI RH95 and p95 of CHM was consistent across the diverse ecosystems covered in all 40 NEON sites in Appendix A.

3.3.2. GEDI Model Correction Factor

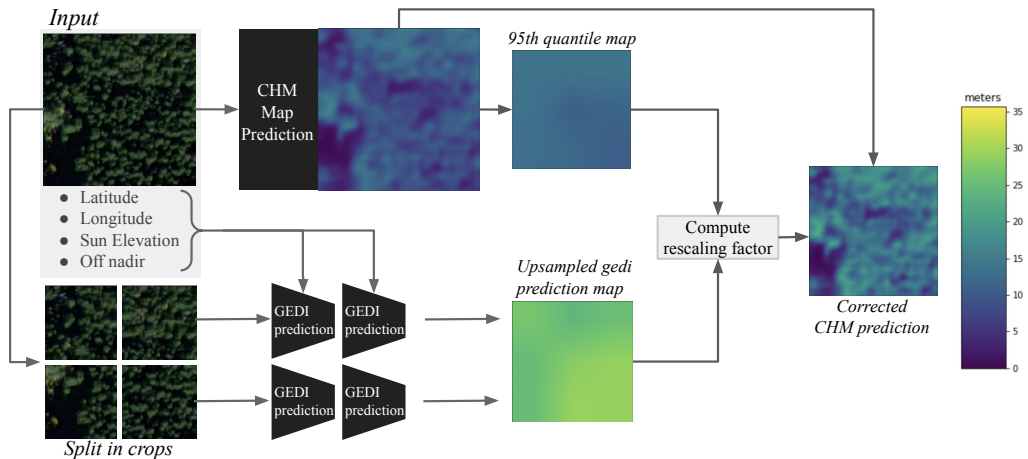


Figure 3: Post processing step using GEDI predictions at test time. We used the GEDI model to correct our CHM predictions at test time, by computing a dense scaling factor, and multiply it pointwise with the CHM prediction map.

Given an input RGB image, x , we combined the outputs of the ALS and GEDI models by computing a correction factor $\gamma(x)$, so that the novel prediction, $C'(x)$ was related to the ALS model CHM, $C(x)$, as follows:

$$C'(x) = \gamma(x) \odot C(x) \quad (2)$$

where

$$\gamma(x) = (1 + G(x))/(1 + (Q(x)_{95})). \quad (3)$$

Here $G(x)$ is the output CHM of our GEDI model and $Q(x)_{95}$ is the 95th percentile of the ALS model CHM in meters, computed over the exact same 128×128 pixel input regions as the input to the GEDI model in $G(x)$. We used the ratio in Equation 3 rather than $G(x)/Q(x)_{95}$ to down-weight noisy model estimates near zero canopy height. Since $G(x)$ and $Q(x)$ are lower

resolution than $C(x)$, the correction factor was upsampled to match the resolution of the ALS CHM, $C(x)$. During the upsampling, the correction factor was smoothed with a 20 pixel sigma (σ) Gaussian kernel to prevent sharp transitions, and clipped between 0.5 and 2 to avoid drastic rescaling. A schematic of the process is shown in Figure 3.

4. Results

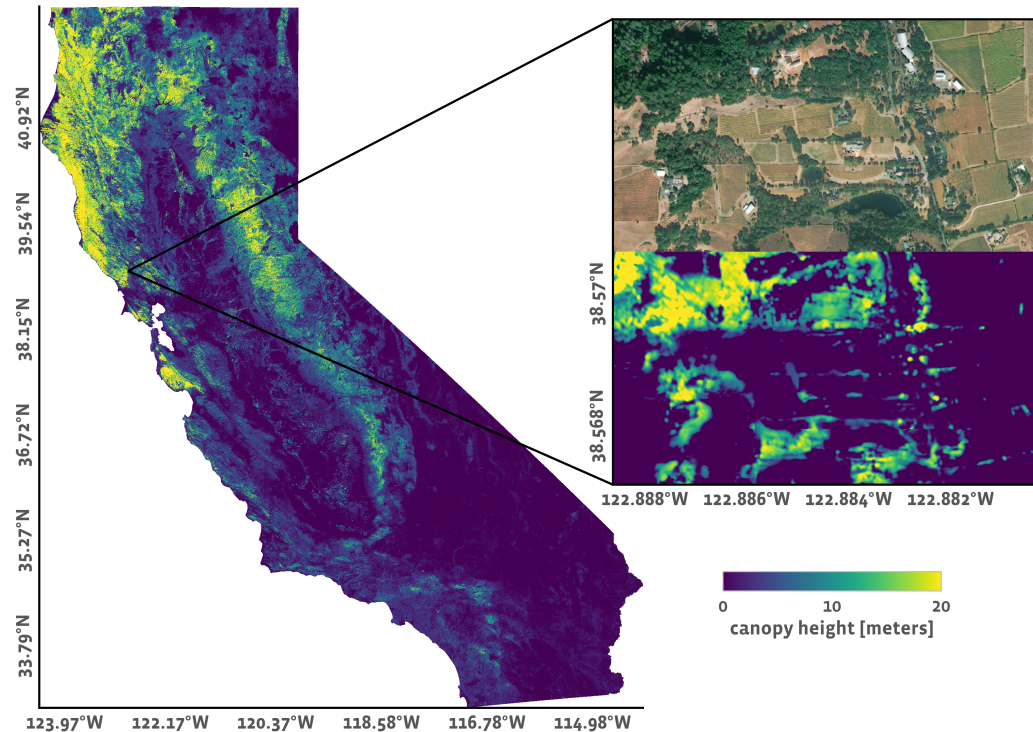


Figure 4: Canopy Height Map (CHM) for the state of California, inset showing zoomed in region with input RGB imagery.

We generated approximately 0.5 meter CHMs for the State of California, USA (Figure 4) and São Paulo (Figure 5). In California, 39 percent of the area uses Maxar imagery observed in 2020, and 90 percent within the years spanning 2018 to 2020. In São Paulo, 63 percent of the area was observed in 2019, and 94 percent within the years spanning 2017-2019. Small regions of the canopy height predictions are visualized in Figure 6. Visual comparisons of our canopy height maps with those of Lang et al. (2022a) and Potapov et al.

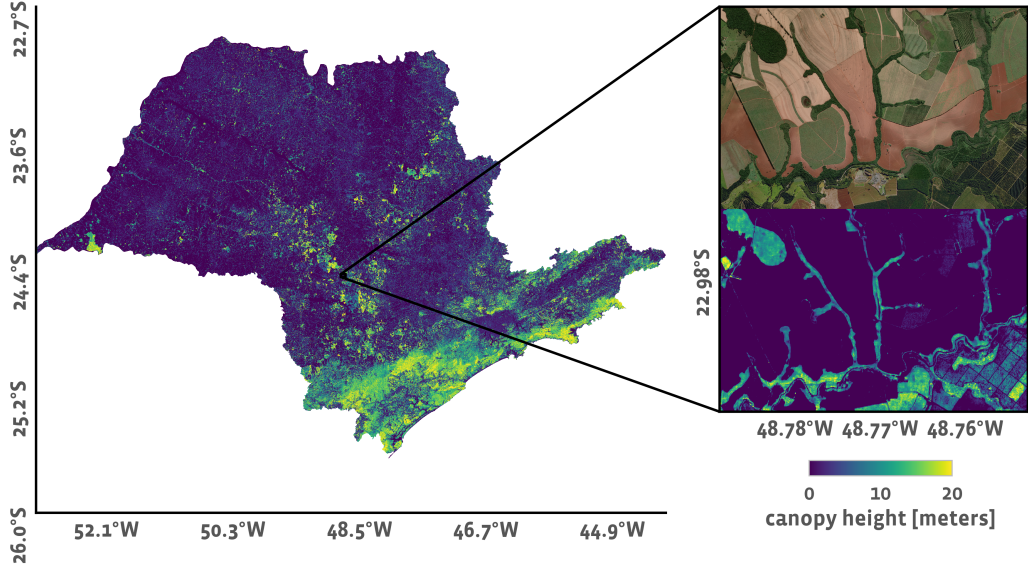


Figure 5: Canopy Height Map (CHM) for the state of São Paulo, inset showing zoomed in region with input RGB imagery.

(2021) are shown in Figure 7. We have added the full resolution dataset to AWS Opendata programs, in the form of cloud optimized geotiffs (COGS) with associated cutlines and image acquisition dates³. Additionally, these datasets are visible on a Google Earth Engine public url⁴.

We evaluate the model performance against a variety of metrics, reflecting the wide range of potential applications of the dataset. We divide the metrics into three broad classes: (1.) Metrics which primarily evaluate the accuracy of canopy height maps, which we call canopy height metrics (Section 4.1), (2.) Metrics which primarily evaluate the accuracy of image segmentation into tree or no tree pixels, which we call segmentation metrics (Section 4.2), and (3.) Metrics which reflect the model’s ability to correctly identify tree instances and estimate tree heights, which we call tree instance and tree height metrics (Section 4.6).

The set-aside validation dataset of ALS canopy height maps described in Section 2 serves as the primary dataset for all three types of metrics. For

³<https://registry.opendata.aws/dataforgood-fb-forests/>

⁴<https://wri-datalab.earthengine.app/view/submeter-canopyheight>

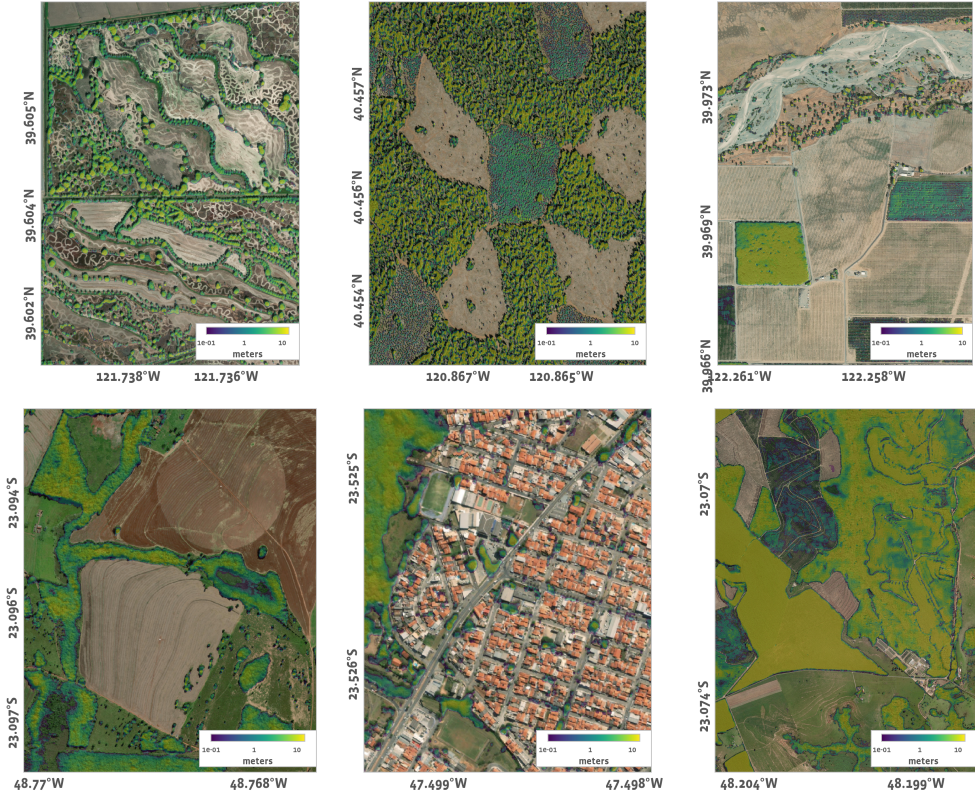


Figure 6: Selected sample regions from the canopy height predictions (log scale), overlaid on the input Maxar imagery (RGB). Canopy height prediction below 0.1 meter is transparent. The top row corresponds to regions in California and the bottom row, São Paulo.

the segmentation metrics, we also evaluate the model predictions against a dataset of human-annotated labels independently labeled by photo-interpretation of Maxar imagery.

4.1. Canopy height metrics

We compared the predicted canopy height maps with aerial lidar data in terms of mean absolute error (MAE), and R^2 -block (R^2). The R^2 -block score is the coefficient of determination, which we computed on cropped images with a resolution of 50×50 pixels ($\sim 30 \times 30$ meters). This score better reflects the local accuracy of CHMs and provides a more direct performance comparison to lower resolution models, however, averages across blocks of

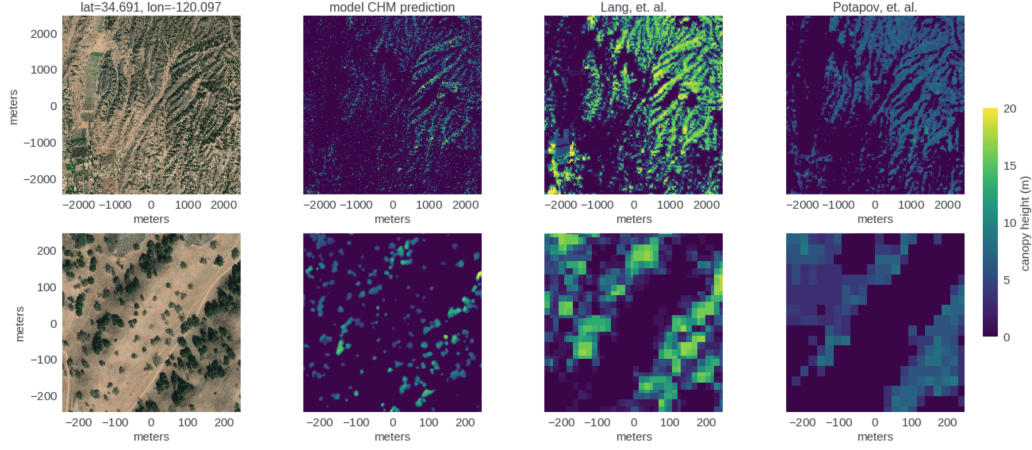


Figure 7: Comparison of our CHM (second column) with that of Lang et al. (2022a) (third column) and Potapov et al. (2021) (fourth column).

this resolution do not provide a good indicator of the edge accuracy of the produced maps, which can be a desirable property for downstream tasks such as segmentation. We separately report edge accuracy in Section 4.2.

Table 1 presents a quantitative validation of backbone models, including ResUNet, the self-supervised finetuned model (SSL), and the SSL model combined with the GEDI correction step (SSL+GEDI). We note the improved performance of the SSL model compared to the ResUNet in our NEON test, CA-Brande and France datasets. The improvement of the SSL model is less clear in the São Paulo dataset, but we find the SSL model performs better in segmentation metrics (Section 4.2). The GEDI correction brings additional improvement to the SSL model, as shown in the SSL + GEDI row in Table 1. Finally, Figure 8 shows 2D-histograms of the SSL+GEDI model predictions vs the set-aside validation ALS-derived canopy height averaged over ~ 30 m blocks and the corresponding pixel MAE and block- R^2 scores.

	NEON test		CA-Brande		São Paulo		France		Average	
	MAE	R^2								
ResUNet	3.52	0.49	0.64	0.73	5.16	0.45	3.92	0.59	3.31	0.56
SSL	2.82	0.66	0.63	0.69	6.02	0.12	3.2	0.71	3.17	0.55
SSL + GEDI	2.77	0.67	0.61	0.75	5.64	0.23	2.99	0.80	3.00	0.61

Table 1: Canopy Height Metrics. R^2 corresponds to $\sim 30 \times 30$ meter block R^2 .

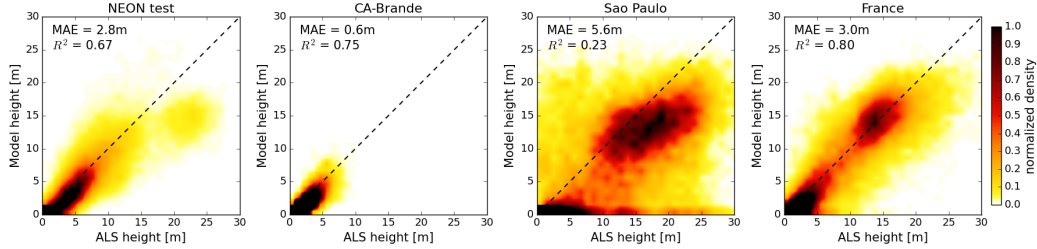


Figure 8: Block ($\sim 30m \times 30m$) aggregated SSL + GEDI model predictions compared to ALS ground truth measurements for different set-aside validation datasets. Colormap density is normalized to the 99.6th percentile of the heatmaps.

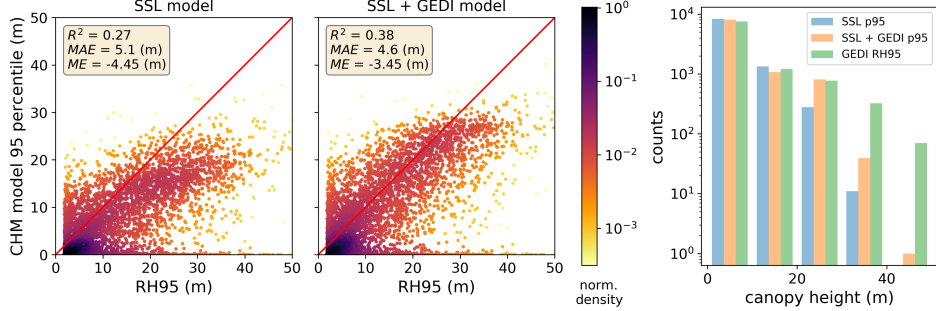
4.1.1. Quantitative comparison of CHM model with GEDI RH95 data

The ALS set-aside validation datasets used in the previous section are limited in both total area and geographic coverage. In this section, we leverage the global coverage of the GEDI dataset to validate our CHM models. As described in Section 3.3.1, CHM maps can be connected to GEDI RH95 metrics by taking the 95th percentile. In this analysis, we draw 1×10^4 GEDI samples globally in the set-aside validation split the same way as in training the GEDI model, i.e., weighted proportional to the square root of the inverse sample size of its RH95 bin. In Fig. 9a, we show the scatter plot and histogram of the 128×128 pixels ($76m \times 76m$) block 95th percentile vs. the measured GEDI RH95. In Fig. 9b, we analyze the difference of the CHM p95 and the GEDI RH95 with respect to the referenced GEDI RH95 heights.

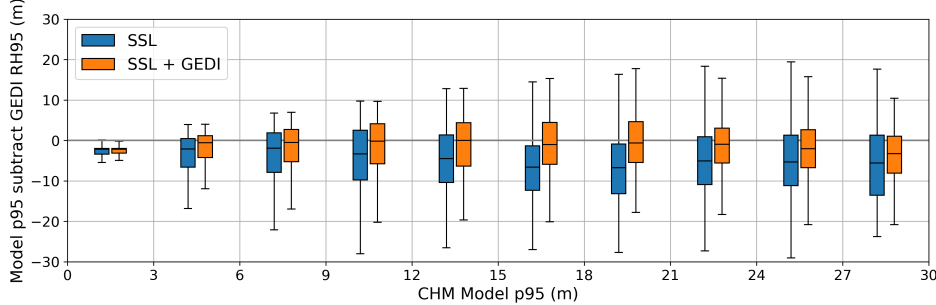
We find that the p95 of the CHM model are biased low against the GEDI RH95 values and adding the GEDI correction to the CHM model significantly reduces the bias. There is a slight positive bias in the GEDI RH95 data due to the terrain slope (Lang et al., 2022a), which can be observed from the existence of a minimum floor value in the x-axis of Fig. 9a. We use terrain slope (Mapzen, 2017) as one of the input metadata when training the GEDI model (see Section 3.1), while setting the terrain slope to zero during inference. With this setup, we are able to calibrate out the positive bias caused by terrain slope in our GEDI model.

4.2. Segmentation metrics

In addition to the canopy height metrics discussed in Section 4.1, we compute a number of metrics that reflect the ability of the model to correctly assign individual pixels as vegetation. CHMs are converted into binary masks



(a) MAE: mean absolute error. ME: mean error. R^2 : Coefficient of determination.



(b)

Figure 9: Global model evaluation on held-out GEDI data. (a) p95 of block ($76m \times 76m$) model CHM predictions compared to the measured GEDI RH95 metrics. Left: the SSL model. Center: the SSL model with GEDI correction. Right: the histogram of the CHM p95 and GEDI RH95. (b) Difference between the p95 of block model CHM predictions and the measured GEDI RH95 metrics w.r.t model CHM predictions. Negative values indicate that the model estimates are lower than the GEDI RH95 values.

by thresholding height values of at least five meters (5m) as tree canopy extent. Table 2 shows the pixel user’s and producer’s accuracy values (also known as precision and recall, respectively) for pixels labeled as trees. Table 2 also shows the Intersection Over Union (IOU) for the binary masks, which is calculated as the average of IOU for pixels labeled as tree and the IOU for pixels labeled as ground.

Additionally, we introduce an Edge Error (EE) metric that computes the ratio of the sum of the absolute difference between edges from predicted and ground truth CHM, normalized by the sum of detected edges in both maps. Scores range between 0 and 1, where lower scores indicate improved accuracy along patch edges. In Table 2, the edge error is computed over all set-aside validation datasets. We detail the formula with a figure illustrating

the behavior of this metric in Appendix E.

	NEON test		CA-Brande		São Paulo		France		All
	U/P	IOU	U/P	IOU	U/P	IOU	U/P	IOU	EE
ResUNet	0.74/ 0.76	0.63	0.71/ 0.62	0.73	0.90/ 0.86	0.67	0.81/0.73	0.61	0.55
SSL	0.82 /0.70	0.60	0.83 /0.40	0.64	0.91/0.79	0.59	0.90 /0.80	0.66	0.55
SSL + GEDI	0.81/0.70	0.58	0.78/0.50	0.71	0.92 /0.80	0.60	0.88/ 0.84	0.66	0.53

Table 2: Segmentation metrics. U/P corresponds to pixel user’s / producer’s accuracy of the tree class. IOU to the average of tree & no tree IOU class scores. EE: Edge error.

4.2.1. Tree detection metrics evaluated against human annotated validation data

We compiled human-annotated validation labels for tree detection (binary classification of tree vs no-tree) across 8,903 Maxar thumbnail images. Human annotators were instructed to label any trees above one meter (1m) tall and with a canopy diameter of more than three meters (3m). Annotators were to include standing dead trees and tree-like shrubs, but exclude any grasslands, row crops, lawns, or otherwise vegetative ground cover whose peak height is estimated to be less than 1m from the ground surface. To create the model binary masks for the annotated dataset, we thresholded the model CHM at 1m.

The geographic locations for the images in the dataset correspond to randomly sampled GEDI measurement footprints from our global set-aside validation set where the GEDI measurement had RH95 greater than 3 meters, which we enforce to bias the dataset towards vegetated areas. The data is independent of the aerial lidar measurements used to train the model. This human-annotated dataset therefore provided validation of model generalization in terms of tree segmentation performance to new geographic regions. Over the entire dataset, the user’s and producer’s accuracy was 0.88 ± 0.006 and 0.77 ± 0.008 , while the IOU was 0.74 ± 0.006 indicating good agreement with the human annotations, cf. Table 3. Figure 10 shows examples of model predictions and their corresponding annotations.

We additionally calculated user’s and producer’s accuracy by geographic subregion according to the United Nations geoscheme. Bootstrapping with 10,000 iterations was used to calculate uncertainty for tree segmentation accuracy metrics rather than the methods of Stehman (2014) because the cluster sampling approach was used to generate validation data (Olofsson

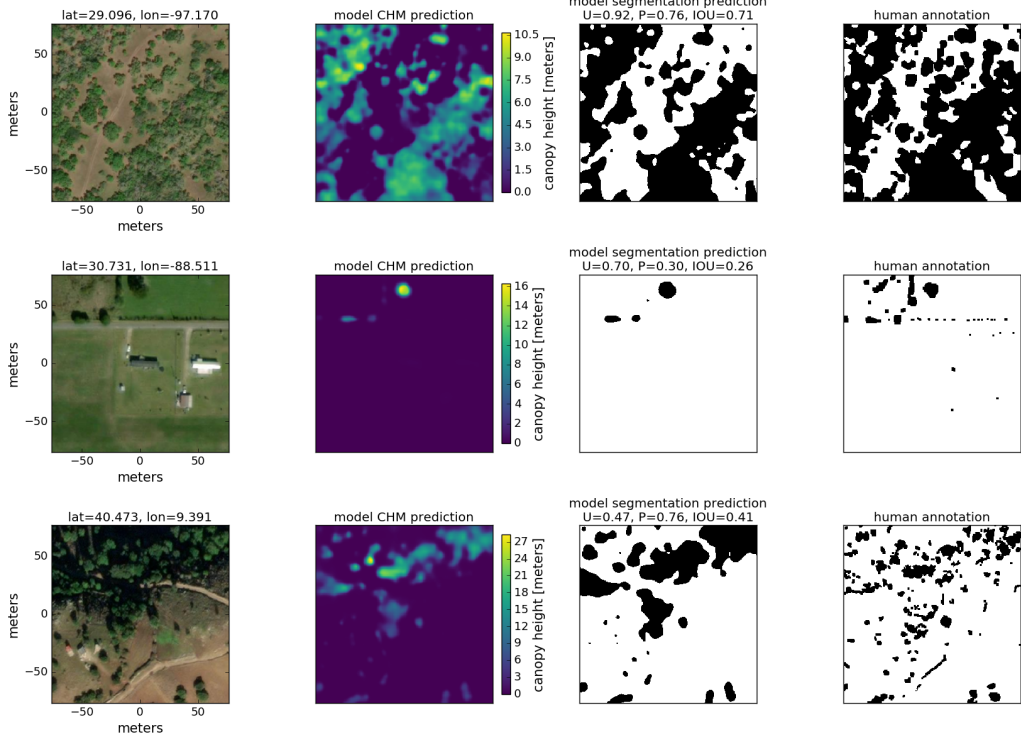


Figure 10: Tree segmentation predictions from the SSL + GEDI model vs human annotated ground truth. U/P corresponds to pixel user's / producer's accuracy of the tree class. The IOU represents the Intersection-Over-Union score for the tree class.

et al. (2014); Mugabowindekwe et al. (2022); Maxwell et al. (2021)). This validation analysis indicated the lowest producer's accuracy in geographic regions with open canopy short trees (Figure 11). We suggest that this may be explained by the degree to which the proposed approach is dependent on the quality (e.g. image and sun angle) of VHR imagery available, and the availability of a growing season (e.g. leaf-on) image, which may be reduced in more remote regions (e.g. Central Asia, Northern Africa). For instance, 74% of the omission errors in South Africa and 67% of the omission errors in Northern Africa had image dates in the respective dry seasons, where tree canopies are less distinguishable (Brandt et al. (2020)).

	Global, Annotated	
	U/P	IOU
ResUNet	0.82/ 0.80	0.72
SSL	0.87/0.71	0.69
SSL + GEDI	0.88 /0.77	0.74

Table 3: Segmentation metrics on global, human annotated dataset. U/P corresponds to pixel user’s / Produces accuracy. IOU to the average of tree & no tree IOU scores.

4.3. Canopy height as a function of plantation age

To evaluate the generated map’s sensitivity to the age-height relationship of tree stands, we utilized the annual 30-meter tree cover gain and loss data from MapBiomas in São Paulo (Azevedo et al. (2018)). We calculated the number of years since the most recent tree cover gain with no subsequent loss event for each image date analyzed. Figure 12 shows a positive relationship ($R^2 = 0.55$) between the number of years since the most recent tree cover gain, and our predicted 95th percentile CHM. For areas with gain events older than seven years, there was no significant age-height relationship, as areas with trees with gain events more than seven years prior to the analysis year had similar height distributions to areas with stable (no gain or loss since 2000) trees. For this analysis, it’s important to note that the tree cover gain year identified in MapBiomas is a lagging indicator of the tree age, since tree cover gain is not immediately recognizable from Landsat imagery.

4.4. Correlation with field data

The Brazilian National Forest Inventory (NFI) consists of systematic field plot inventories of tree count and height (da Luz et al. (2018)). Because the NFI data for São Paulo was not yet available, we additionally generate a CHM of the nearby Espírito Santo state and evaluate its agreement with the NFI data for Espírito Santo. The NFI data analyzed encompassed 1,450 10×10 m subplots within 87 plots positioned within a 20×20 km grid in Espírito Santo. The field data was collected primarily in November and December 2014, and includes the height of each tree within each subplot having a diameter at breast height (DBH) of at least 10 cm. Of the 1,450 initial plots considered, we removed 291 that had tree cover loss since 2014 in the dataset of Hansen et al. (2016). Figure 13 visualizes box plots of the 95th percentile CHM by reference NFI height bins. The overall mean error

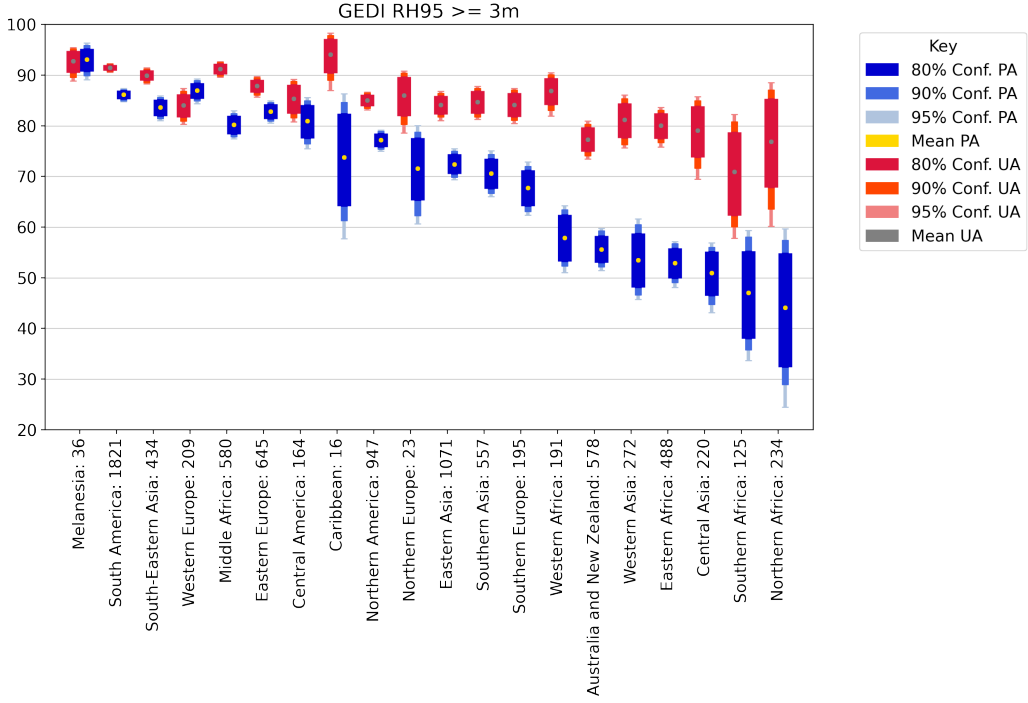


Figure 11: Pixelwise user’s accuracy (UA) and producer’s accuracy (PA) for 8,903 validation plots stratified by geographic sub-region. Error bars represent the 80, 90, and 95 percent confidence intervals as derived from 10,000 bootstrap iterations. Numbers in the x-axis tick labels denote sample size.

(ME) was -0.36 m while the RMSE was 4.35m, with lower error for trees ≤ 15 m (ME = 0.62 m, RMSE = 4.23 m), and higher error for trees > 15 m (ME = -5.9 m, RMSE = 5.73 m).

4.5. Ablation study of model choices

We present in Table 4 an ablation study of different pre-training strategies on the Neon test set. From this ablation study, we selected the SSL model trained on 3.5 million images utilizing the Sigloss loss function, which achieved the highest canopy height accuracy metrics. We refer to this model as the SSL model throughout the paper. Table 4 suggests that pre-training on satellite images gives better results compared to pre-training on ImageNet. We also experimented with different loss functions, and a larger dataset for pre-training. Additional discussion of these trials can be found in Appendix C.

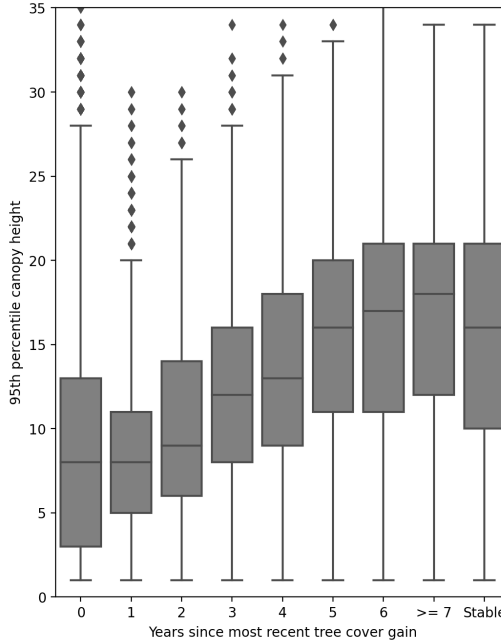


Figure 12: Canopy height estimates for areas with tree cover gain of various ages in São Paulo relative to the imagery year analyzed.

4.6. Individual tree instance and tree height metrics

We evaluate individual tree instance user’s and producer’s accuracy based on the locations and canopy height values around peaks (local maxima) in the predicted and ground truth CHM maps. These metrics complement the canopy height metrics discussed above and highlight the ability of our high resolution model to detect individual trees of different heights. In contrast to canopy height, tree height is more closely tied to the allometric equations linked to biomass.

Our method examines the canopy height maps around the peak location and not just exactly at the peak location, making it more robust to the registration mismatches between the model output and ALS ground truth from orthorectification of the satellite imagery and the effects of the off-nadir view angles on model predictions. This is especially important when trying to determine whether a small tree matches in the model output and ALS ground truth as small trees may only be a few pixels wide.

Due to errors in geo-registration, and the difficulty in labeling tree instances in a canopy height map (especially in regions with closed tree canopy),

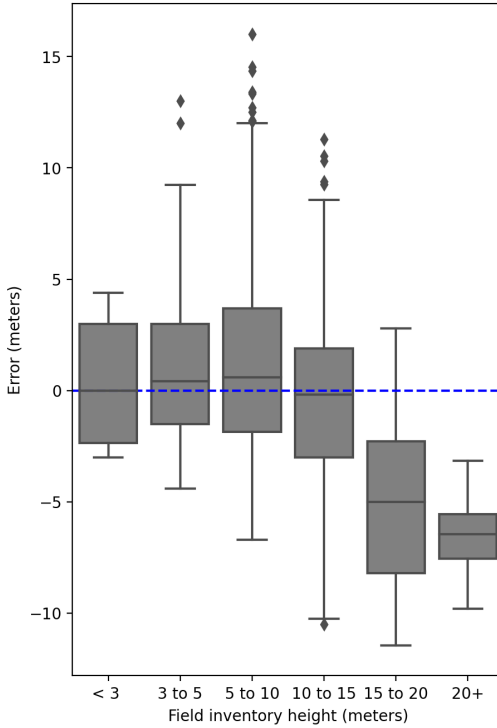


Figure 13: CHM error compared to reference tree height as indicated in the Brazilian National Forest Inventory for Espirito Santo.

it is important to note these metrics are not rigorous instance segmentation metrics such as ones computed against instance labeled ground truth segmentation masks. Nevertheless, they provide useful information about how well the proposed model can detect trees of a particular height, which cannot be directly inferred from the canopy height raster metrics such as the mean absolute error or user’s and producer’s accuracy at the pixel level. The full details of the algorithm are described in Appendix B.

Figure 14 presents a sample visualization of peak detection and true positive, false positive, and false negative classifications. Figure 15 shows the user’s and producer’s accuracy vs. the (binned) tree height across three set-aside validation datasets. The general observation is that user’s and producer’s accuracy vary by region, and that generally individual user’s and producer’s accuracy are greater than 0.8 for trees taller than 10m but begin to noticeably decrease for trees smaller than 10m tall. In certain favorable environments, such as the CA-Brande dataset in central California where

NEON test set					
	model size	pre-training dataset	MAE	R^2 -block	EE
ResUNet	ResNet18	IN1k	3.52	0.49	0.63
SSL-IN1k	ViT large	IN1k	3.37	0.52	0.59
SSL-IN22k	ViT huge	IN22k+	2.92	0.63	0.49
SSL	ViT large	Sat 3.5M	2.82	0.66	0.51

Table 4: Comparison of results with SSL pre-training on different datasets and to the best ResUNet strategy. IN: ImageNet. Sat: dataset described in Section 2.3.2. Note that the SSL results are non GEDI corrected in this table, “SSL” corresponding to the second row of Table 1.

trees are generally isolated and easy to distinguish, the model is capable of achieving user’s/producer’s accuracy of 0.73/0.36 for tree heights between 1 – 3m tall and user’s/producer’s accuracy = 0.91/0.55 for tree heights between 3 – 5m tall.

4.7. Qualitative comparison of models

Although we have attempted to capture the performance of each model qualitatively with the included metrics, we note that visual inspection often leads to additional insights. Therefore, we additionally present a few examples of maps produced by our various models. Figure 16 compares the results with a ResUNet and SSL based strategies. We observe that the ResUNet model sometimes predicts zeros values in large areas, making its predictions less reliable than the SSL results.

5. Discussion

Our proposed method provides a novel approach to estimating canopy height from sub-meter satellite imagery. We demonstrate the effectiveness of self-supervised learning, dense vision transformers, as well as rescaling high-resolution canopy height maps from a model trained on Maxar and ALS data with low-resolution canopy height maps from a model trained on Maxar and GEDI data. In contrast to Lang et al. (2022a), which downscale the 25-meter GEDI data to generate 10-meter canopy height maps by only considering Sentinel-2 pixels at the centroid of each GEDI pixel, our approach uses a GEDI-based canopy height map to rescale an ALS-based model of canopy height map. While both Lang et al. (2022a) and Potapov et al. (2021) only

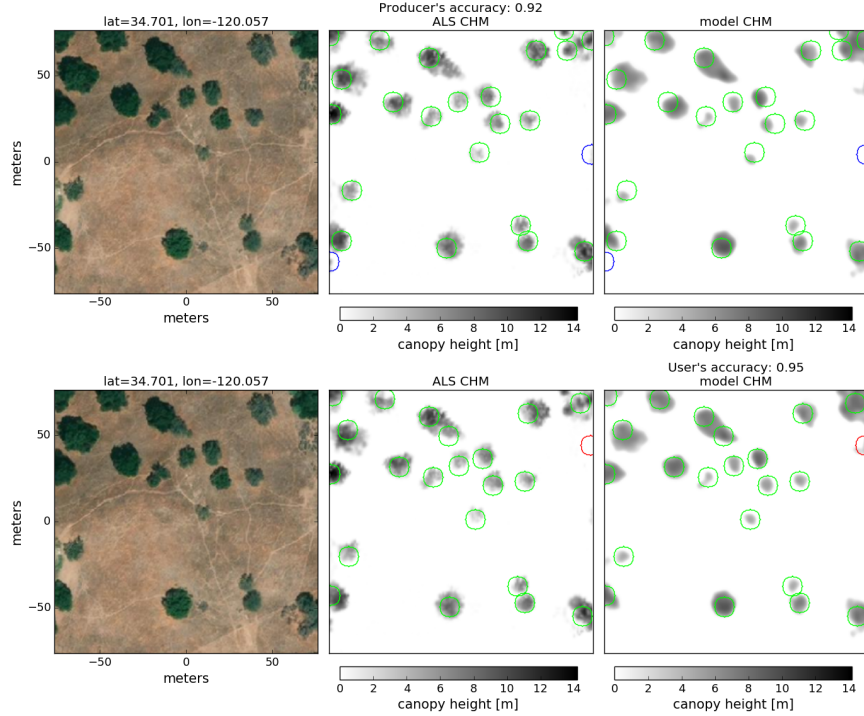


Figure 14: Individual tree instance user’s and producer’s accuracy calculation. The top row shows peak locations in the ALS CHM (producer’s calculation) and the bottom row shows peak locations in the SSL + GEDI model CHM (users calculation). Green circles represent true positives, blue circles represent false negatives, and red circles represent false positives.

utilize ALS data to validate their generated maps, we directly model the relationship between Maxar imagery and ALS data, enabling the mapping of sub-GEDI scale canopy height variability, often times at a per-tree level.

Generalization. To assess the generalization ability of our approach to other input imagery, we measure model performance using airborne imagery at inference. Table 5 shows the MAE and block R^2 scores on NEON input RGB imagery. The SSL model more than doubles the R^2 of the ResUNet baseline. Figure 17 displays an example. For inference, we resized the NEON aerial images to match the size of corresponding satellite image, and apply a normalization of the aerial image to match the color histogram of the satellite imagery. Details about image normalization are provided in Appendix F. Despite changes in color intensity, image angle, and sun angle, our approach

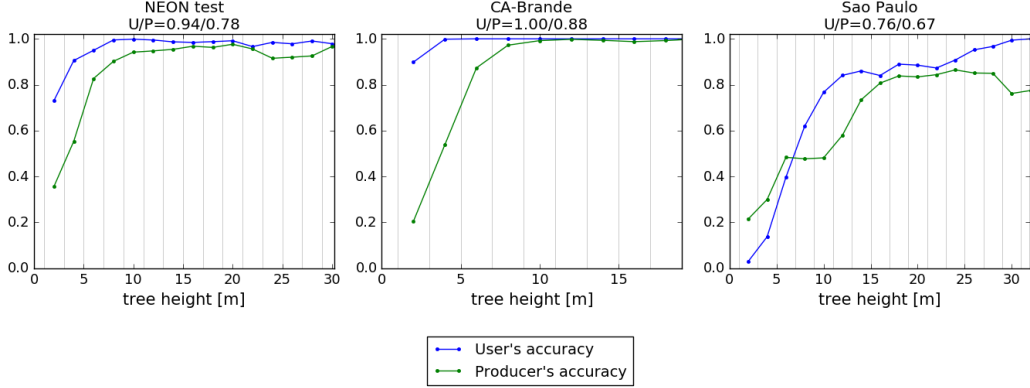


Figure 15: Individual tree instance user’s and producer’s accuracy vs tree height across set-aside validation datasets, calculated using the SSL + GEDI model. U/P indicates user’s/producer’s accuracy.

manages to generate predictions with consistent visual quality. We compare these results to another baseline, fine-tuning a decoder using our pretrained SSL features on Neon RGBs. While this model leads to low MAE scores, our model fully trained on satellite imagery improves the block R^2 accuracy: this is due to inaccurate predictions of the aerial model in areas of low canopy height. An explanation for this may come from the advantage of off-nadir views of Satellite imagery, while aerial image contains less cues for height prediction with more nadir angles. From an application point of view, the robustness of SSL predictions without the need to retrain models on new lidar datasets is very interesting.

Neon test - aerial				
Pretraining dataset	Fine-tuning dataset	MAE	block R^2	
ResUNet	INet	3.80	0.22	
SSL	Sat. images	3.11	0.54	
SSL	Sat. images	2.64	0.47	

Table 5: CHM prediction accuracy on NEON test dataset using aerial input images as inputs. Trained on satellite images only, the SSL approaches demonstrates generalization abilities.

Segmentation. Previous research applying deep learning image segmentation approaches to map trees in high-resolution imagery, such as Brandt et al.

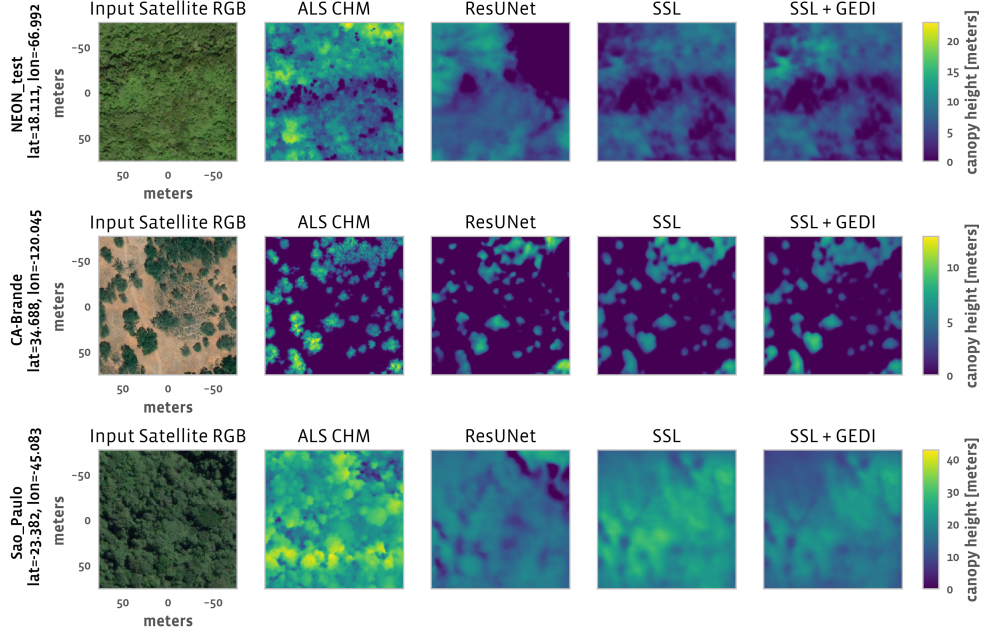


Figure 16: Qualitative comparison between different models for example imagery. Left: Input Maxar “thumbnail” image, 256×256 pixels, in local tangent plane coordinate system. Second from left: ALS CHM image, in same projection and pixelization. Right columns: Model CHMs.

(2020) and Mugabowindekwe et al. (2022) have utilized a U-Net model (Ronneberger et al. (2015)) and entirely hand-labeled reference data. Focusing in Rwanda, Mugabowindekwe et al. (2022) map carbon stock estimates for individual trees by developing empirical relationships between crown area and carbon, finding that half of the national tree carbon stock is located outside of natural forests. In comparison to these approaches, our results suggest that incorporating SSL can improve model generalizability for vegetation structure mapping, in line with various research demonstrating the effectiveness of SSL in other domains. Further, our results demonstrate the relative advantage of vision transformers over CNN models for vegetation structure mapping. Additionally, our per-pixel height predictions combine the predictive quality of height for assessing biomass as demonstrated in Lang et al. (2022b) and Potapov et al. (2021) with the predictive quality of crown area

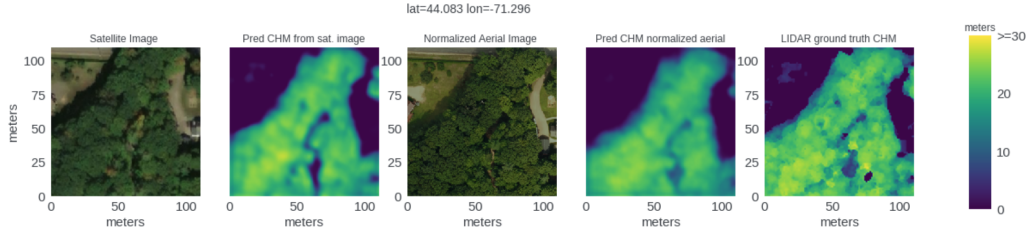


Figure 17: Generalisation of our SSL approach. Even if trained on Satellite images, inference on airborne images does not seem to suffer from a domain shift.

for assessing biomass as demonstrated in Mugabowindekwe et al. (2022) and Skole et al. (2021).

Monitoring. Tree canopy height is an important variable for assessing the status of conservation and restoration projects. The height of individual trees is often recorded over time when assessing the progress of forest restoration sites (Viani et al. (2018), Vallauri et al. (2005)). Tree height and tree canopy area are both predictive variables for allometric modeling of tree biomass and removal factors under the REDD+ program. For both of these land use management applications, wall-to-wall, high resolution data on tree height is directly useful for assessing the status of project activities, as well as for identifying potential areas to implement projects, identifying counterfactuals, and tracking project additionality (Camarretta et al. (2020)).

Limitations. The production of high-resolution canopy height maps from optical imagery has challenges and associated limitations. Foremost, the availability of recent ALS training data is limited in geographic scope. While the utilization of self-supervised learning and the GEDI-based corrective model improve generalization and reduce test error, increased geographic availability of ALS remains necessary to further validate the proposed maps in new geographies.

The generated maps are limited by variation in input imagery, particularly by variation in view angle, sun angle, acquisition times and dates, and optical aerosol. Additionally, terrain slope appears to influence predicted height, since it affects the length of shadow an individual tree casts. At present, the ability to conduct tree height change detection assessments is limited by the need for improved input image processing to better align these differences between image pairs.

As indicated in Section 4.4, we have found a bias towards underestimating canopy height for taller trees, particularly in Brazilian states of São Paulo and Espírito Santo. This effect may be due to the relative scarcity of the highest heights in the training data, and needs further subsequent investigation.

6. Conclusions

This study presents high-resolution canopy height maps at a jurisdictional scale based on high resolution (Maxar) optical imagery trained on aerial lidar and calibrated with spaceborn lidar (GEDI) data using latest advances from self-supervised learning and vision transformers.

We demonstrate quantitatively and qualitatively the relative advantages of large-scale self-supervised learning for pretraining the encoder, using multi-source training data, and the use of a dense transformer as the decoder. Compared to existing canopy height maps, the presented data better captures tree structure variability at small spatial scales. Such high resolution maps of canopy height can improve the monitoring of forest degradation, restoration, and forest carbon dynamics. The next steps include (a) developing and validating allometrically-derived high-resolution woody carbon data and (b) testing and validating the utility of the proposed approach for the operation monitoring of tree growth.

7. Acknowledgments

We would like to thank Ben Weinstein for helpful discussions regarding the NEON dataset. We thank Andi Gros and Saikat Basu for their technical advice. We would like to thank Shmulik Eisenmann, Patrick Louis, Lee Francisco, Leah Harwell, Eric Alamillo, Sylvia Lee, Patrick Nease, Alex Pompe and Shawn Mcguire for their project support.

Appendix A. List of sites used in training / calibration / validation

The NEON sites during training / calibration are : SJER, SOAP, TEAK, BART, DSNY, HARV, JERC, OSBS, DELA, GRSM, LENO, MLBS, BLAN, CLBJ, KONZ, NOGP, SCBI, TALL, UKFS, WOOD, ABBY, BONA, DEJU, JORN, MOAB, OAES, ONAQ, SERC, SRER, UNDE, WREF, HEAL, LAJA, RMNP, PUUM.

The set-aside validation dataset, "NEON test", contains the following NEON sites: CUPE, REDB, WLOU, HOPB, GUAN.

The set-aside validation sets of the France dataset are: Dommartin les cuiseaux, Comps, Viuz en Sallaz, Izenave, Manosque, Forcalquier, Borne.

To ensure repeatability of our approach, we provide a complete list of CHM files used during training/calibration at: https://dataforgood-fb-data.s3.amazonaws.com/forests/v1/NEON_training_images.csv

Appendix B. Tree Instance user's and producer's Accuracy

Algorithm 1 describes the full procedure for computing the tree instance user's and producer's accuracy from a pair of model and ALS canopy height maps. The calculation for user's accuracy is the same as for the calculation for producer's accuracy but with ALS and model CHM values swapped. We only apply the tree detection method when at least 1% of the ALS CHM contains ground level data (pixels at least 5m away from any ALS CHM value that is higher than 1m), in order to set the background noise level which determines the tree detection thresholds as described in more detail below. Computing the detection threshold in this way penalizes producer's accuracy in cases where the model makes predictions in areas without trees and penalizes the user's accuracy if the model fails to make predictions in areas with trees. We define the minimum height of a tree to be 1m.

Algorithm 1 Tree instance user's and producer's accuracy calculation

1. Peak Finding

Find peaks (local maxima) within the model/ALS CHM $> 1\text{m}$ tall and separated by at least 5m.

2. Detection threshold

Compute the mean, μ , and standard-deviation, σ , of the ALS/model CHM values in regions where all model/ALS predictions within 5m are less than 1m in height. Set detection threshold = $\max(1, \mu + 2\sigma)$.

3. Tree detection

For each peak detected in step 1, compute the max height of the ALS/model CHM around the peak location (within a 5m radius). Classify the peak as a true positive if the max height $>$ detection threshold, and as a false positive/negative otherwise.

Appendix C. Alternate Loss Function Ablation

We compare in Table C.6 results of models trained with L1 loss or Sigloss, and using different sizes of pretraining dataset: one with 3.5×10^6 images (referred to as "SSL 3.5M" in Table C.6) and one with 18×10^6 images ("SSL 18M"). The Sigloss (sl) leads to better results for datasets of low canopy, however the best performance in term of height prediction is reached by the SSL model with L1 loss, and various amount of pre-training data. Considering sharpness with the Edge Error (EE) metric, the SSL baseline (SSL 3.5M sl) is by far the best model. The SSL18M model with Sigloss is bringing a compromise between edge accuracy and error in height prediction. For picking the final model, the preference was given to the model predicting the sharpest maps (SSL 3.5M sl).

	Neon test			CA Brande			São Paulo			France			Average		
	MAE	R^2	EE												
ResUNet	3.52	0.49	0.63	0.64	0.73	0.48	5.16	0.45	0.54	3.92	0.59	0.56	3.31	0.56	0.55
SSL 18M sl	2.52	0.76	0.62	0.67	0.78	0.50	5.85	0.17	0.65	3.01	0.75	0.64	3.01	0.62	0.60
SSL 18M L1	2.68	0.68	0.65	0.66	0.73	0.49	4.98	0.45	0.65	2.81	0.83	0.66	2.78	0.67	0.61
SSL 3.5M sl	2.82	0.66	0.52	0.63	0.69	0.48	6.02	0.12	0.60	3.20	0.71	0.58	3.17	0.55	0.55
SSL 3.5M + GEDI	2.77	0.67	0.51	0.61	0.75	0.46	5.64	0.23	0.57	2.99	0.80	0.56	3.00	0.61	0.53

Table C.6: CHM prediction accuracy metrics with different architectures, backbone and loss functions.

Appendix D. Training Details

Our code uses Pytorch 1.9.0 with Cuda 10.2.

SSL pretraining. We refer the reader Oquab et al. (2023) for the SSL pre-training phase details. We only changed the image normalization parameters from ImageNet parameters to match the standard deviation and mean color intensities of our 3.5M dataset. The unsupervised pretraining took a little less than three days on two 8-GPUs Voltas. Instead of the standard ImageNet normalization parameters, we computed the mean and standard deviation on our dataset of 3.5M trees. The encoder contains 303 M of parameters.

SSL fine-tuning. The training of CHM prediction from SSL features takes a few hours using a single GPU, depending on the number of steps performed. During this step, we kept the weights of the SSL encoder frozen and only train the DPT model. Our DPT decoder for the SSL 3.5M model was trained for

140k steps using a Cosine learning rate schedule (from 1×10^{-8} to 1×10^{-4}) with a linear warmup step for 12k iterations. We used a batch size of 2. This decoder model contains 34.2 M of parameters.

Appendix E. Edge Error Metric

The edge error score is given by Algorithm 2. Figure E.18 illustrates how this metric is computed in an example.

Algorithm 2 Edge Error metric

1. Edge detection

$E(\hat{c})$: Sobel detector on predicted CHM maps \hat{c} .

$E(c)$: Sobel detector on GT CHM maps c .

2. Compute normalization factor $d = (\sum_i |E(\hat{c}_i)|) + (\sum_i |E(c_i)|)$.

3. Edge error score

If $d > 0$

$$\text{score} = \frac{1}{d} \sum_i |E(\hat{c}_i) - E(c_i)|.$$

Else

$$\text{score} = 0.$$

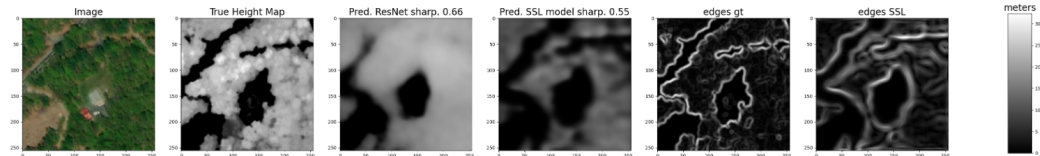


Figure E.18: Illustration of edge error metric for two results: the ResUNet edge error score is 0.66 in this example, the score of the SSL model is 0.55, computed using difference of the prediction and ground truth edge maps appearing in the two images at the right.

Appendix F. Normalization for inference on aerial imagery

An image normalization step is necessary to improve the SSL inference performance on aerial images, when training only on Satellite imagery. We perform a histogram normalization of the aerial images (i.e. normalize the RGB channels of the aerial image to the p5-p95 distribution of the satellite image). This makes the color balance much more similar, leading to better performance for the SSL model. The satellite image is taken through much

more atmosphere and we expect it to be less blue on average, because of preferential scattering of shorter wavelengths. Noting I the satellite image, A the original aerial image, we first compute for each color channel i and each image X the 5% percentile $p_5(X)_i$ and 95% percentile $p_{95}(X)_i$. Then, the normalized aerial image is given by

$$A_i = (A_i - p_5(A)_i) * \frac{p_{95}(I)_i - p_5(I)_i}{p_{95}(A)_i - p_5(A)_i} + p_5(I)_i.$$

We only apply this normalization to the SSL model trained on satellite imagery. Applying this normalization to the ResUNet model alters the results as well.

References

Almeida, D., Broadbent, E., Zambrano, A., Wilkinson, B., Ferreira, M., Chazdon, R., Meli, P., Gorgens, E., Silva, C., Stark, S., Valbuena, R., Papa, D., Brancalion, P., 2019a. Monitoring the structure of forest restoration plantations with a drone-lidar system. *International Journal of Applied Earth Observation and Geoinformation* 79, 192–198. URL: <https://www.sciencedirect.com/science/article/pii/S0303243418311954>, doi:<https://doi.org/10.1016/j.jag.2019.03.014>.

Almeida, D., Stark, S., Chazdon, R., Nelson, B., Cesar, R., Meli, P., Gorgens, E., Duarte, M., Valbuena, R., Moreno, V., Mendes, A., Amazonas, N., Gonçalves, N., Silva, C., Schiatti, J., Brancalion, P., 2019b. The effectiveness of lidar remote sensing for monitoring forest cover attributes and landscape restoration. *Forest Ecology and Management* 438, 34–43. URL: <https://www.sciencedirect.com/science/article/pii/S037811271831819X>, doi:<https://doi.org/10.1016/j.foreco.2019.02.002>.

de Almeida, D.R.A., Broadbent, E.N., Ferreira, M.P., Meli, P., Zambrano, A.M.A., Gorgens, E.B., Resende, A.F., de Almeida, C.T., do Amaral, C.H., Corte, A.P.D., Silva, C.A., Romanelli, J.P., Prata, G.A., de Almeida Papa, D., Stark, S.C., Valbuena, R., Nelson, B.W., Guillemot, J., Féret, J.B., Chazdon, R., Brancalion, P.H., 2021. Monitoring restored tropical forest diversity and structure through uav-borne hyperspectral and lidar fusion. *Remote Sensing of Environment* 264, 112582. URL: <https://www.sciencedirect.com/science/article/pii/S0034425721003023>, doi:<https://doi.org/10.1016/j.rse.2021.112582>.

de Almeida, D.R.A., Stark, S.C., Valbuena, R., Broadbent, E.N., Silva, T.S.F., de Resende, A.F., Ferreira, M.P., Cardil, A., Silva, C.A., Amazonas, N., Zambrano, A.M.A., Brancalion, P.H.S., 2020. A new era in forest restoration monitoring. *Restoration Ecology* 28, 8–11. URL: <https://onlinelibrary.wiley.com/doi/abs/10.1111/rec.13067>. doi:<https://doi.org/10.1111/rec.13067>.

Azevedo, T., Souza, C., Zanin Shimbo, J., Alencar, A., 2018. Mapbiomas initiative: Mapping annual land cover and land use changes in brazil from 1985 to 2017.

Badgley, G., Freeman, J., Hamman, J.J., Haya, B., Trugman, A.T., Anderegg, W.R., Cullenward, D., 2022. Systematic over-crediting in California's forest carbon offsets program. *Global Change Biology* 28, 1433–1445. doi:[10.1101/2021.04.28.441870](https://doi.org/10.1101/2021.04.28.441870).

Bhat, S.F., Alhashim, I., Wonka, P., 2021. Adabins: Depth estimation using adaptive bins, in: Proceedings of the IEEE/CVF Conference on Computer Vision and Pattern Recognition, pp. 4009–4018.

Brande, K., 2021. 3d fuel structure in relation to prescribed fire, ca 2020. national center for airborne laser mapping (ncalm). distributed by opentopography. URL: <https://doi.org/10.5069/G9C53J18>. accessed: 2023-02-15.

Brandt, M., Tucker, C.J., Kariryaa, A., Rasmussen, K., Abel, C., Small, J., Chave, J., Rasmussen, L.V., Hiernaux, P., Diouf, A.A., Kergoat, L., Mertz, O., Igel, C., Gieseke, F., Schöning, J., Li, S., Melocik, K., Meyer, J., Sinno, S., Romero, E., Glennie, E., Montagu, A., Dendoncker, M., Fensholt, R., 2020. An unexpectedly large count of trees in the West African Sahara and Sahel. *Nature* .

Camarretta, N., Harrison, P.A., Bailey, T., Potts, B., Lucieer, A., Davidson, N., Hunt, M., 2020. Monitoring forest structure to guide adaptive management of forest restoration: a review of remote sensing approaches. *New Forests* 51, 573–596. URL: <https://doi.org/10.1007/s11056-019-09754-5>, doi:[10.1007/s11056-019-09754-5](https://doi.org/10.1007/s11056-019-09754-5).

Caron, M., Touvron, H., Misra, I., Jégou, H., Mairal, J., Bojanowski, P., Joulin, A., 2021. Emerging properties in self-supervised vision transformers, in: Proceedings of the IEEE/CVF International Conference on Computer Vision, pp. 9650–9660.

Cook-Patton, S.C., Leavitt, S.M., Gibbs, D., Harris, N.L., Lister, K., Anderson-Teixeira, K.J., Briggs, R.D., Chazdon, R.L., Crowther, T.W., Ellis, P.W., Griscom, H.P., Herrmann, V., Holl, K.D., Houghton, R.A., Larrosa, C., Lomax, G., Lucas, R., Madsen, P., Malhi, Y., Paquette, A., Parker, J.D., Paul,

K., Routh, D., Roxburgh, S., Saatchi, S., van den Hoogen, J., Walker, W.S., Wheeler, C.E., Wood, S.A., Xu, L., Griscom, B.W., 2020. Mapping carbon accumulation potential from global natural forest regrowth. *Nature* 585, 545–550. URL: <https://doi.org/10.1038/s41586-020-2686-x>.

Csillik, O., Kumar, P., Mascaro, J., O'Shea, T., Asner, G.P., 2019. Monitoring tropical forest carbon stocks and emissions using planet satellite data. *Scientific Reports* 9, 17831. URL: <https://doi.org/10.1038/s41598-019-54386-6>.

Cuni-Sanchez, A., Sullivan, M.J.P., Platts, et al, P., 2021. High aboveground carbon stock of African tropical montane forests. *Nature* 596, 536–542. doi:10.1038/s41586-021-03728-4.

Dalagnol, R., Phillips, O.L., Gloor, E., Galvão, L.S., Wagner, F.H., Locks, C.J., Aragão, L.E.O.C., 2019. Quantifying canopy tree loss and gap recovery in tropical forests under low-intensity logging using vhr satellite imagery and airborne lidar. *Remote Sensing* 11. URL: <https://www.mdpi.com/2072-4292/11/7/817>, doi:10.3390/rs11070817.

Dos-Santos, M., Keller, M., Morton, D., 2019. Lidar surveys over selected forest research sites, Brazilian Amazon, 2008-2018. ORNL DAAC, Oak Ridge, Tennessee, USA. URL: https://daac.ornl.gov/CMS/guides/LiDAR_Forest_Inventory_Brazil.html.

Dosovitskiy, A., Beyer, L., Kolesnikov, A., Weissenborn, D., Zhai, X., Unterthiner, T., Dehghani, M., Minderer, M., Heigold, G., Gelly, S., Uszkoreit, J., Houlsby, N., 2021. An image is worth 16x16 words: Transformers for image recognition at scale, in: 9th International Conference on Learning Representations, ICLR 2021, Virtual Event, Austria, May 3-7, 2021, OpenReview.net. URL: <https://openreview.net/forum?id=YicbFdNTTy>, doi:10.48550/ARXIV.2010.11929.

Dubayah, R., Armston, J., Kellner, J., Duncanson, L., Healey, S., Patterson, P., Hancock, S., Tang, H., Bruening, J., Hofton, M., Blair, J., Luthcke, S., 2022. GEDI L4A footprint level aboveground biomass density, version 2.1. URL: https://daac.ornl.gov/cgi-bin/dsviewer.pl?ds_id=2056, doi:10.3334/ORNLDaac/2056.

Dubayah, R., Blair, J.B., Goetz, S., Fatoyinbo, L., Hansen, M., Healey, S., Hofton, M., Hurt, G., Kellner, J., Luthcke, S., Armston, J., Tang, H., Duncanson, L., Hancock, S., Jantz, P., Marselis, S., Patterson, P.L., Qi, W., Silva, C., 2020. The global ecosystem dynamics investigation: High-resolution laser ranging

of the earth's forests and topography. *Science of Remote Sensing* 1, 100002. URL: <https://www.sciencedirect.com/science/article/pii/S2666017220300018>, doi:<https://doi.org/10.1016/j.srs.2020.100002>.

Duncanson, L., Neuenschwander, A., Hancock, S., Thomas, N., Fatoyinbo, T., Simard, M., Silva, C.A., Armston, J., Luthcke, S.B., Hofton, M., Kellner, J.R., Dubayah, R., 2020. Biomass estimation from simulated GEDI, ICESat-2 and NISAR across environmental gradients in Sonoma County, California. *Remote Sensing of Environment* 242, 111779. URL: <https://www.sciencedirect.com/science/article/pii/S0034425720301498>, doi:<https://doi.org/10.1016/j.rse.2020.111779>.

Friedlingstein, P., Jones, M.W., O'Sullivan, M., Andrew, R.M., Hauck, J., Peters, G.P., Peters, W., Pongratz, J., Sitch, S., Le Quéré, C., Bakker, D.C.E., Canadell, J.G., Ciais, P., Jackson, R.B., Anthoni, P., Barbero, L., Bastos, A., Bastrikov, V., Becker, M., Bopp, L., Buitenhuis, E., Chandra, N., Chevallier, F., Chini, L.P., Currie, K.I., Feely, R.A., Gehlen, M., Gilfillan, D., Gkritzalis, T., Goll, D.S., Gruber, N., Gutekunst, S., Harris, I., Haverd, V., Houghton, R.A., Hurt, G., Ilyina, T., Jain, A.K., Joetzjer, E., Kaplan, J.O., Kato, E., Klein Goldewijk, K., Korsbakken, J.I., Landschützer, P., Lauvset, S.K., Lefèvre, N., Lenton, A., Lienert, S., Lombardozzi, D., Marland, G., McGuire, P.C., Melton, J.R., Metzl, N., Munro, D.R., Nabel, J.E.M.S., Nakaoka, S.I., Neill, C., Omar, A.M., Ono, T., Peregon, A., Pierrot, D., Poulter, B., Rehder, G., Resplandy, L., Robertson, E., Rödenbeck, C., Séférian, R., Schwinger, J., Smith, N., Tans, P.P., Tian, H., Tilbrook, B., Tubiello, F.N., van der Werf, G.R., Wiltshire, A.J., Zaehle, S., 2019. Global carbon budget 2019. *Earth System Science Data* 11, 1783–1838. URL: <https://essd.copernicus.org/articles/11/1783/2019/>, doi:[10.5194/essd-11-1783-2019](https://doi.org/10.5194/essd-11-1783-2019).

Gibril, M.B.A., Shafri, H.Z.M., Al-Ruzouq, R., Shanableh, A., Nahas, F., Al Mansoori, S., 2023. Large-scale date palm tree segmentation from multiscale uav-based and aerial images using deep vision transformers. *Drones* 7. URL: <https://www.mdpi.com/2504-446X/7/2/93>, doi:[10.3390/drones7020093](https://doi.org/10.3390/drones7020093).

Hancock, S., Armston, J., Hofton, M., Sun, X., Tang, H., Duncanson, L.I., Kellner, J.R., Dubayah, R., 2019. The GEDI simulator: A large-footprint waveform lidar simulator for calibration and validation of spaceborne missions. *Earth and Space Science* 6, 294–310. URL: <https://onlinelibrary.wiley.com/doi/full/10.1029/2018EA000506><https://onlinelibrary.wiley.com/doi/abs/10.1029/2018EA000506><https://agupubs.onlinelibrary.wiley.com/doi/10.1029/2018EA000506>, doi:[10.1029/2018EA000506](https://doi.org/10.1029/2018EA000506).

Hansen, M.C., Krylov, A., Tyukavina, A., Potapov, P.V., Turubanova, S., Zutta, B., Ifo, S., Margono, B., Stolle, F., Moore, R., 2016. Humid tropical forest disturbance alerts using landsat data. *Environmental Research Letters* 11, 034008. URL: <https://dx.doi.org/10.1088/1748-9326/11/3/034008>, doi:10.1088/1748-9326/11/3/034008.

Harris, N.L., Gibbs, D.A., Baccini, A., Birdsey, R.A., de Bruin, S., Farina, M., Fatoyinbo, L., Hansen, M.C., Herold, M., Houghton, R.A., Potapov, P.V., Suarez, D.R., Roman-Cuesta, R.M., Saatchi, S.S., Slay, C.M., Turubanova, S.A., Tyukavina, A., 2021. Global maps of twenty-first century forest carbon fluxes. *Nature Climate Change* 11, 234–240. URL: <https://doi.org/10.1038/s41558-020-00976-6>, doi:10.1038/s41558-020-00976-6.

He, K., Chen, X., Xie, S., Li, Y., Dollár, P., Girshick, R., 2022. Masked autoencoders are scalable vision learners, in: *Proceedings of the IEEE/CVF Conference on Computer Vision and Pattern Recognition*, pp. 16000–16009.

IGN, 2021. LidarHD: Une cartographie 3D du sol et du sursol de la France. <https://geoservices.ign.fr/lidarhd/>.

Khosravipour, A., Skidmore, A.K., Isenburg, M., Wang, T., Hussin, Y.A., 2014. Generating pit-free canopy height models from airborne lidar. *Photogrammetric Engineering and Remote Sensing* 80, 863–872. doi:10.14358/PERS.80.9.863.

Lang, N., Jetz, W., Schindler, K., Wegner, J.D., 2022a. A high-resolution canopy height model of the earth. URL: <https://arxiv.org/abs/2204.08322>, doi:10.48550/ARXIV.2204.08322.

Lang, N., Kalischek, N., Armston, J., Schindler, K., Dubayah, R., Wegner, J.D., 2022b. Global canopy height regression and uncertainty estimation from GEDI LIDAR waveforms with deep ensembles. *Remote Sensing of Environment* 268, 112760. URL: <https://www.sciencedirect.com/science/article/pii/S0034425721004806>, doi:<https://doi.org/10.1016/j.rse.2021.112760>.

Li, W., Niu, Z., Shang, R., Qin, Y., Wang, L., Chen, H., 2020. High-resolution mapping of forest canopy height using machine learning by coupling icesat-2 lidar with sentinel-1, sentinel-2 and landsat-8 data. *International Journal of Applied Earth Observation and Geoinformation* 92, 102163. URL: <https://www.sciencedirect.com/science/article/pii/S030324342030026X>, doi:<https://doi.org/10.1016/j.jag.2020.102163>.

Li, Z., Wang, X., Liu, X., Jiang, J., 2022. Binsformer: Revisiting adaptive bins for monocular depth estimation. *arXiv preprint arXiv:2204.00987*.

Liu, S., Brandt, M., Nord-Larsen, T., Chave, J., Reiner, F., Lang, N., Tong, X., Ciais, P., Igel, C., Li, S., Mugabowindekwe, M., Saatchi, S., Yue, Y., Chen, Z., Fensholt, R., 2023. The overlooked contribution of trees outside forests to tree cover and woody biomass across Europe. doi:10.21203/rs.3.rs-2573442/v1.

Luo, W., Li, Y., Urtasun, R., Zemel, R., 2016. Understanding the effective receptive field in deep convolutional neural networks. *Advances in neural information processing systems* 29. URL: <https://arxiv.org/abs/1701.04128>, doi:10.48550/ARXIV.1701.04128.

da Luz, N.B., Garrastazu, M.C., Rosot, M.A.D., Maran, J.C., de Oliveira, Y.M.M., Franciscon, L., Cardoso, D.J., de Freitas, J.V., 2018. Inventário florestal nacional do brasil - uma abordagem em escala de paisagem para monitorar e avaliar paisagens florestais. *Pesquisa Florestal Brasileira* 38. URL: <https://pfb.cnpf.embrapa.br/pfb/index.php/pfb/article/view/1493>, doi:10.4336/2018.pfb.38e201701493.

Mapzen, 2017. Amazon. Terrain Tiles on AWS. <https://registry.opendata.aws/terrain-tiles>.

Maxwell, A.E., Warner, T.A., Guillén, L.A., 2021. Accuracy assessment in convolutional neural network-based deep learning remote sensing studies—part 2: Recommendations and best practices. *Remote Sensing* 13. URL: <https://www.mdpi.com/2072-4292/13/13/2591>, doi:10.3390/rs13132591.

Mugabowindekwe, M., Brandt, M., Chave, J., Reiner, F., Skole, D.L., Kariyaa, A., Igel, C., Hiernaux, P., Ciais, P., Mertz, O., et al., 2022. Nation-wide mapping of tree-level aboveground carbon stocks in rwanda. *Nature Climate Change* , 1–7.

National Ecological Observatory Network (NEON), 2022. Ecosystem structure (dp3.30015.001). URL: <https://data.neonscience.org/data-products/DP3.30015.001>.

Olofsson, P., Foody, G.M., Herold, M., Stehman, S.V., Woodcock, C.E., Wulder, M.A., 2014. Good practices for estimating area and assessing accuracy of land change. *Remote Sensing of Environment* 148, 42–57. URL: <https://www.sciencedirect.com/science/article/pii/S0034425714000704>, doi:<https://doi.org/10.1016/j.rse.2014.02.015>.

Oquab, M., Darcet, T., Moutakanni, T., Vo, H., Szafraniec, M., Khalidov, V., Fernandez, P., Haziza, D., Massa, F., El-Nouby, A., Assran, M., Ballas, N.,

Galuba, W., Howes, R., Huang, P.Y., Li, S.W., Misra, I., Rabbat, M., Sharma, V., Synnaeve, G., Xu, H., Jegou, H., Mairal, J., Labatut, P., Joulin, A., Bojanowski, P., 2023. Dinov2: Learning robust visual features without supervision. [arXiv:2304.07193](https://arxiv.org/abs/2304.07193).

Popkin, G., 2015. The hunt for the world's missing carbon. *Nature* 523, 20–22. doi:10.1038/523020a.

Popkin, G., 2015. The hunt for the world's missing carbon. *Nature* 523, 20–22. doi:10.1038/523020a.

Potapov, P., Li, X., Hernandez-Serna, A., Tyukavina, A., Hansen, M.C., Komareddy, A., Pickens, A., Turubanova, S., Tang, H., Silva, C.E., Armston, J., Dubayah, R., Blair, J.B., Hofton, M., 2021. Mapping global forest canopy height through integration of GEDI and Landsat data. *Remote Sensing of Environment* 253, 112165. URL: <https://www.sciencedirect.com/science/article/pii/S0034425720305381>, doi:<https://doi.org/10.1016/j.rse.2020.112165>.

Ranftl, R., Bochkovskiy, A., Koltun, V., 2021. Vision transformers for dense prediction. International Conference on Computer Vision .

Reed, C.J., Gupta, R., Li, S., Brockman, S., Funk, C., Clipp, B., Candido, S., Uyttendaele, M., Darrell, T., 2022. Scale-MAE: A scale-aware masked autoencoder for multiscale geospatial representation learning. *arXiv preprint arXiv:2212.14532* .

Ronneberger, O., Fischer, P., Brox, T., 2015. U-net: Convolutional networks for biomedical image segmentation, in: Medical Image Computing and Computer-Assisted Intervention–MICCAI 2015: 18th International Conference, Munich, Germany, October 5–9, 2015, Proceedings, Part III 18, Springer. pp. 234–241.

Schwartz, M., Ciais, P., Ottle, C., Wigneron, J.P., De Truchis, A., Li, S., Brandt, M., Fensholt, R., D'Aspremont, A., Vega, C., Baghdadi, N., Fayad, I., Morneau, F., Guyon, D., Dayau, S., 2021. High Resolution Biomass and Height Maps of the Landes Forest (France) based on GEDI, Sentinel-1 and Sentinel-2 data : a Deep Learning Approach, in: AGU Fall Meeting Abstracts, pp. B45H–1719.

Silva, C.A., Duncanson, L., Hancock, S., Neuenschwander, A., Thomas, N., Hofton, M., Fatoyinbo, L., Simard, M., Marshak, C.Z., Armston, J., Lutchke, S., Dubayah, R., 2021. Fusing simulated GEDI, ICESat-2 and NISAR data for regional aboveground biomass mapping. *Remote Sensing of Environment* 253, 112234. URL: <https://www.sciencedirect.com/science/article/pii/S0034425720306076>, doi:<https://doi.org/10.1016/j.rse.2020.112234>.

Sirko, W., Kashubin, S., Ritter, M., Annkah, A., Bouchareb, Y.S.E., Dauphin, Y.N., Keysers, D., Neumann, M., Cissé, M., Quinn, J., 2021. Continental-scale building detection from high resolution satellite imagery. CoRR abs/2107.12283. URL: <https://arxiv.org/abs/2107.12283>.

Skole, D.L., Samek, J.H., Dieng, M., Mbow, C., 2021. The contribution of trees outside of forests to landscape carbon and climate change mitigation in west Africa. *Forests* 12. URL: <https://www.mdpi.com/1999-4907/12/12/1652>, doi:10.3390/f12121652.

Stehman, S.V., 2014. Estimating area and map accuracy for stratified random sampling when the strata are different from the map classes. *International Journal of Remote Sensing* 35, 4923–4939. URL: <https://doi.org/10.1080/01431161.2014.930207>, doi:10.1080/01431161.2014.930207, arXiv:<https://doi.org/10.1080/01431161.2014.930207>.

Stephenson, N.L., Das, A.J., Condit, R., Russo, S.E., Baker, P.J., Beckman, N.G., Coomes, D.A., Lines, E.R., Morris, W.K., Rüger, N., Álvarez, E., Blundo, C., Bunyavejchewin, S., Chuyong, G., Davies, S.J., Duque, Á., Ewango, C.N., Flores, O., Franklin, J.F., Grau, H.R., Hao, Z., Harmon, M.E., Hubbell, S.P., Kenfack, D., Lin, Y., Makana, J.R., Malizia, A., Malizia, L.R., Pabst, R.J., Pongpattananurak, N., Su, S.H., Sun, I.F., Tan, S., Thomas, D., van Mantgem, P.J., Wang, X., Wiser, S.K., Zavala, M.A., 2014. Rate of tree carbon accumulation increases continuously with tree size. *Nature* 507, 90–93. URL: <https://doi.org/10.1038/nature12914>, doi:10.1038/nature12914.

Tesfay, F., Moges, Y., Asfaw, Z., 2022. Woody species composition, structure, and carbon stock of coffee-based agroforestry system along an elevation gradient in the moist mid-highlands of southern ethiopia. *International Journal of Forestry Research* 2022, 1–12. doi:10.1155/2022/4729336.

Vallauri, D., Aronson, J., Dudley, N., Vallejo, R., 2005. Monitoring and Evaluating Forest Restoration Success. Springer New York, New York, NY. pp. 150–158. URL: https://doi.org/10.1007/0-387-29112-1_21, doi:10.1007/0-387-29112-1_21.

Viani, R.A.G., Barreto, T.E., Farah, F.T., Rodrigues, R.R., Brancalion, P.H.S., 2018. Monitoring young tropical forest restoration sites: How much to measure? *Tropical Conservation Science* 11, 1940082918780916. URL: <https://doi.org/10.1177/1940082918780916>, doi:10.1177/1940082918780916.

Wang, W., Tang, C., Wang, X., Zheng, B., 2022. A ViT-based multiscale feature fusion approach for remote sensing image segmentation. *IEEE Geoscience and Remote Sensing Letters* 19, 1–5. doi:10.1109/LGRS.2022.3187135.

Weinstein, B.G., Graves, S.J., Marconi, S., Singh, A., Zare, A., Stewart, D., Bohlman, S.A., White, E.P., 2021. A benchmark dataset for canopy crown detection and delineation in co-registered airborne RGB, LiDAR and hyperspectral imagery from the National Ecological Observation Network. *PLoS Comput Biol.* .

West, T.A.P., Börner, J., Sills, E.O., Kontoleon, A., 2020. Overstated carbon emission reductions from voluntary redd+ projects in the brazilian amazon. *Proceedings of the National Academy of Sciences* 117, 24188–24194. URL: <https://www.pnas.org/doi/abs/10.1073/pnas.2004334117>, doi:10.1073/pnas.2004334117.

Xu, Z., Zhang, W., Zhang, T., Yang, Z., Li, J., 2021. Efficient transformer for remote sensing image segmentation. *Remote Sensing* 13. URL: <https://www.mdpi.com/2072-4292/13/18/3585>, doi:10.3390/rs13183585.

Yanai, R.D., Wayson, C., Lee, D., Espejo, A.B., Campbell, J.L., Green, M.B., Zukswert, J.M., Yoffe, S.B., Aukema, J.E., Lister, A.J., Kirchner, J.W., Gamarra, J.G.P., 2020. Improving uncertainty in forest carbon accounting for redd+ mitigation efforts. *Environmental Research Letters* 15, 124002. URL: <https://dx.doi.org/10.1088/1748-9326/abb96f>, doi:10.1088/1748-9326/abb96f.

Zhang, Z., Liu, Q., Wang, Y., 2017. Road extraction by deep residual U-Net. *CoRR* abs/1711.10684. URL: <http://arxiv.org/abs/1711.10684>.

Zhou, J., Wei, C., Wang, H., Shen, W., Xie, C., Yuille, A., Kong, T., 2022. ibot: Image bert pre-training with online tokenizer. *ICLR* .